GEOPHYSICS, VOL. 75, NO. 3 (MAY-JUNE 2010); P. B115–B136, 25 FIGS., 2 TABLES.
10.1190/1.3427637

Case History

Creating realistic models based on combined forward modeling and tomographic inversion of seismic profiling data

Ivan Koulakov[1], Tatiana Stupina[1], and Heidrun Kopp[2]

ABSTRACT

Amplitudes and shapes of seismic patterns derived from tomographic images often are strongly biased with respect to real structures in the earth. In particular, tomography usually provides continuous velocity distributions, whereas major velocity changes in the earth often occur on first-order interfaces. We propose an approach that constructs a realistic structure of the earth that combines forward modeling and tomographic inversion (FM&TI). Using available a priori information, we first construct a synthetic model with realistic patterns. Then we compute synthetic times and invert them using the same tomographic code and the same parameters as in the case of observed data processing. We compare the reconstruction result with the tomographic image of observed data inversion. If a discrepancy is observed, we correct the synthetic model and repeat the FM&TI process. After several trials, we obtain similar results of synthetic and observed data inversion. In this case, the derived synthetic model adequately represents the real structure of the earth. In a working scheme of this approach, we three authors used two different synthetic models with a realistic setup. One of us created models, but the other two performed the reconstruction with no knowledge of the models. We discovered that the synthetic models derived by FM&TI were closer to the true model than the tomographic inversion result. Our reconstruction results from modeling marine data acquired in the Musicians Seamount Province in the Pacific Ocean indicate the capacity and limitations of FM&TI.

INTRODUCTION

The increased data density along seismic profiles progressively requires automating processing and interpretation tools. The interpretation results then provide rich information about the structure of the earth's interior for the depths, depending on the scale of the experiment — from a few meters' depth in engineering and exploration tasks (e.g., Martí et al., 2008; Yordkayhun et al., 2009) to crustal and upper mantle structures in deep seismic sounding studies (e.g., Nielsen and Thybo, 2009; Palomeras et al., 2009, among recent successful examples). Kinematic modeling schemes based on traveltime information provided by refracted seismic rays represent the dominant approach to wide-angle data modeling. In some studies, the traveltimes of reflected rays are used to constrain the a priori model and to perform joint inversion of refracted and reflected traveltimes (e.g., Korenaga et al., 2000; Sallarès et al., 2003).

There are two basic schemes for modeling refraction data: forward kinematic modeling and tomographic inversion, which usually are performed independently and in some cases complement each other (e.g., Nielsen and Thybo, 2009). Forward kinematic modeling consists of computing traveltimes in different velocity models. The aim of this approach is to find a velocity model that provides the best fit to the observed traveltimes (e.g., Luetgert, 1992; Zelt and Smith, 1992). The velocity distribution is usually adjusted manually and strongly depends on the scientist's experience. In many cases, a comparison of calculated traveltimes with the observed times provides an ambiguous, nonunique solution. It is fairly difficult to formalize this process and render it automatically. Therefore, the alternative tomographic inversion approach is more popular because it seems to be less dependent on the subjective input of the user.

During the last few decades, several different tomographic approaches have been developed for noncommercial active source profiling (e.g., Hole, 1992; Zelt and Barton, 1998; Korenaga et al., 2000; Hobro et al., 2003). Most of the codes used in practice (e.g., FAST code; Zelt and Barton, 1998) are based on first-arrival data. However, some codes use later phases (e.g., Tomo2D, Korenaga et al., 2000) and inhomogeneous starting models based on existing a priori information. We should also mention the FMTOMO code (Rawlinson and Urvoy, 2006), which includes a wide range of possibilities such as passive and active schemes, teleseismic data, direct and multiple reflecting phases, inversion for 3D velocity distribution, interface geometry, and source coordinates.

Manuscript received by the Editor 20 June 2009; revised manuscript received 17 November 2009; published online 26 May 2010.
[1]Institute of Petroleum Geology and Geophysics, Novosibirsk, Russia. E-mail: koulakoviy@ipgg.nsc.ru; E-mail: stupinata@ipgg.nsc.ru.
[2]Leibniz Institute of Marine Sciences, IFM-GEOMAR, Kiel, Germany. hkopp@ifm-geomar.de.

However, the tomographic approach has some obvious limitations, which makes the interpretation of the results quite intricate. First, in most cases, the tomography results provide a continuous velocity-depth distribution without first-order velocity contrasts. Given a starting model with predefined velocity interfaces, these cannot be shifted by the relative velocity anomalies obtained during first-arrival tomography. In most applied studies, the output of the tomographic inversion is a continuous velocity model, presented by contour lines. At the same time, however, it is common to base the geologic-tectonic interpretation on the distribution of the main petrophysical interfaces (e.g., basement, Moho), which seem to follow some contour lines (e.g., 6.0 and 7.8 km/s). This is an obvious contradiction that must be considered the main shortcoming of the tomographic approach in refraction seismic techniques.

In many cases, it is useful to predefine the starting model based on a priori information of the local study area. However, the final solution would be controlled mostly by this preconditioning of the starting model. As a consequence, it is difficult to judge if any similarities between the input model and the final output model adequately represent the natural setting. Just analyzing the rms values of traveltime residuals after inversion is not sufficient. For some parts of the study area, the solution may be well founded, resulting in small average rms values, whereas other parts of the model (especially areas with a sparse ray coverage) may not be authentic. In addition, in case of insufficient ray coverage, the solution can contain artifacts that are not easily separated from relevant patterns.

Furthermore, the damped tomographic inversion usually biases the shapes and amplitudes of the retrieved patterns with respect to real structures in the earth. It should be admitted that the velocity distribution reported in tomograms is not a direct image of real structures but just a blurred picture. Retrieving the real velocity distribution in the earth is only possible through careful investigating of properties of the tomographic operator.

We propose a new approach, called forward modeling and tomographic inversion (FM&TI), to solve some of these issues. FM&TI consists of six stages:

1) Processing the real data using tomographic inversion
2) Constructing a synthetic model with realistic velocity distribution
3) Computing synthetic traveltimes in this model
4) Processing the synthetic data using the same steps of tomographic inversion and free parameters as in stage 1
5) Comparing the tomograms derived after stages 1 and 4
6) Updating the synthetic model and iteratively performing stages 2–6

The FM&TI approach is based on a newly developed code (Koulakov, 2009b) called PROFIT (profile forward and inverse tomographic modeling), which can be applied for modeling marine and land active seismic profiling data. The code creates user-friendly complex seismic models as input for subsequent forward modeling and inversion. The same strategy can be realized using some other codes.

The approach of finding a probabilistic model based on combined forward modeling and tomographic inversion has been used in 3D passive-source tomographic imaging in central Java (Koulakov et al., 2007), in the Toba caldera (Koulakov et al., 2009b), and for some regional (Koulakov and Sobolev, 2006) and teleseismic (Koulakov et al., 2006) studies. For active-source profiling tomography, FM&TI is novel.

This paper presents the FM&TI approach for 2D refraction active-source data. To show the working ability of this approach, we use synthetic and real data sets that correspond to various geologic settings of different scales and complexity. The first data set is based on a complicated synthetic *Mount* model that may exist, for example, in tunnel exploration (Figure 1a). The second data set, the *Salt* model (Figure 2a), is based on an experiment in the Pre-Caspian area. The presented model is purely synthetic but uses realistic distributions of source-receiver pairs. We simulate two high-velocity salt domes and try to reproduce them using existing synthetic traveltimes. The third data set, *Sea*, consists of a marine profile acquired in the Musicians Seamount Province located north of the Hawaiian Chain in the Pacific Ocean (Freedman and Parsons, 1986; Sager and Pringle, 1987). Data processing is described in detail in Kopp et al. (2003) and in Appendix A.

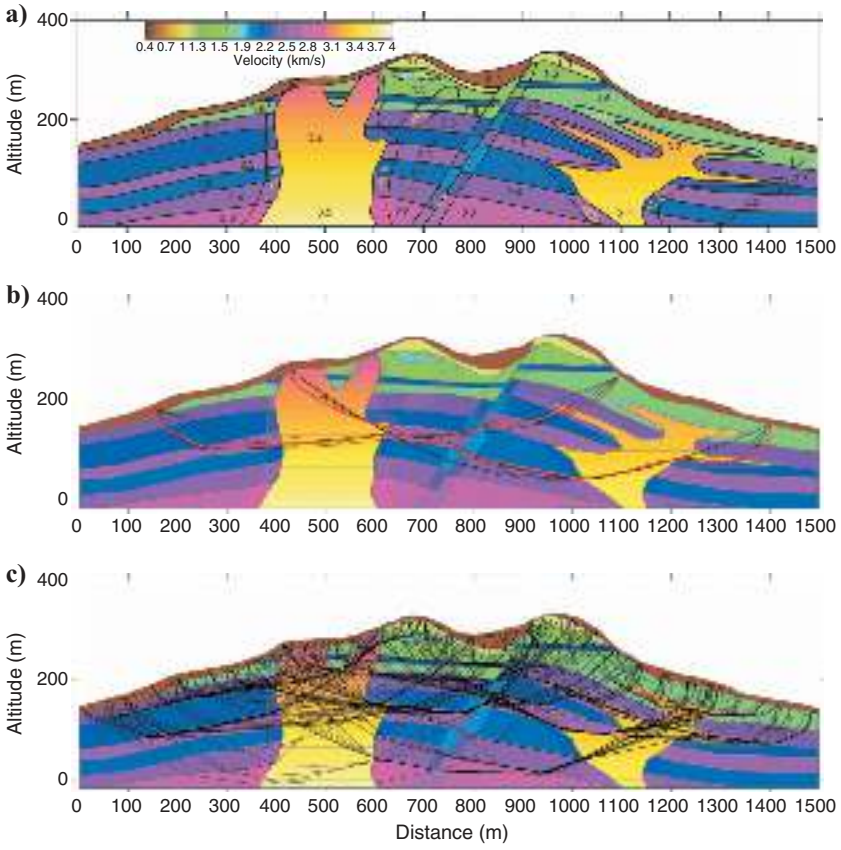

Figure 1. Synthetic Mount model. (a) Velocity definition in the model. Black numbers indicate values of velocities; white numbers are velocity variations in percent. (b) Two examples of ray construction using iterative bending. Black lines depict the evolution of the raypath in iterations; red is the final path. (c) Raypaths for sources and receivers located on the surface; one-tenth of the total ray amount in the synthetic data set is shown.

Results of tomographic modeling of this data set are presented.

The FM&TI approach, which unites the concepts of ray-tracing modeling and tomographic inversion, may provide more reliable and realistic images of the subsurface structure than applying these methods individually.

PROFIT ALGORITHM

General notes

To construct complex synthetic models, to compute traveltimes in 2D velocity distributions, and to perform the tomographic inversion, we have developed the PROFIT code (Koulakov, 2009b). The code consists of two major components. The first comprises the tomographic inversion; it can be used as an independent and separate tomographic code for processing seismic refraction data. The second part of PROFIT is aimed at FM&TI.

The tomographic inversion of observed data using PROFIT is performed by iteratively executing the following steps:

1) Ray trace in the 2D velocity model (starting model in first iteration or updated velocity model after previous iterations).
2) Construct the parameterization grid (first iteration only).
3) Calculate the matrix and inversion.
4) Update the velocity model and return to step 1.

In the following, we describe the most important features of each of these steps.

Ray tracing

The ray tracing used in PROFIT is based on the Fermat principle and consists of finding a path that provides the minimum traveltime between source and receiver. This idea is the basis of the bending method of ray tracing (e.g., Um and Thurber, 1987), which has been widely applied for decades and has evolved as a standard in different practical codes of local earthquake tomography (e.g., Thurber, 1993) and seismic modeling (e.g., Korenaga et al., 2000). Some modifications of the bending method allow for ray tracing in weakly anisotropic models (e.g., Grechka and McMechan, 1996).

We have created an alternative version of the bending algorithm, shown schematically in Figure 3. Finding the path of minimum traveltime consists of consecutively executing several bending regimes. In the initial step (Figure 3a), the intersection point of the ray with the sea bottom (b, the bounce point) is located just beneath the source s. We start from the straight line between b and r and deform it to obtain the minimum traveltime. In the first approximation, the deviation A with respect to the initial straight path is computed according to

$$A(d) = B\cos\left(\pi\frac{d-\frac{D_{\text{tot}}}{2}}{D_{\text{tot}}}\right), \tag{1}$$

where B is the value of bending, d is the distance along the initial path, and D_{tot} is the total length of the initial path between b and r. The value of B is adjusted to obtain the curve $\gamma(B)$, which provides the minimum value of the integral:

$$t = \int_{\gamma(B)} \frac{d\gamma}{V(d)}, \tag{2}$$

where $V(d)$ is the velocity distribution along the ray.

In the second step (Figure 3b), we laterally move b to obtain the minimum value of integral 2. For land observations, this step is omitted because the locations of s and b are identical.

At the next stages (Figure 3c and d), further deviations of the path between b and r are performed iteratively using a formula for bending values:

$$A(d) = \frac{B}{2}\cos\left(2\pi\frac{\frac{d-(D_2-D_1)}{2}}{(D_2-D_1)}\right)+\frac{1}{2}, \tag{3}$$

where D_1 and D_2 correspond to the length along the path in the beginning and at the end of the current segment.

During the first iteration, the bending is performed for the entire segment $b-r$ in a similar way as demonstrated in Figure 3a but using formula 3. In the second iteration (Figure 3c), the path is divided into two segments of equal lengths ($b-m_1$ and m_1-r), and each is bent according to formula 3. After determining the minimum time curve, the entire path is divided into three parts (Figure 3d), and the same approach of bending is performed for segments $b-m_1$, m_1-m_2, and m_2-r. This procedure is repeated for the path divided into four, five, and more parts. The bending terminates when the length of the sections becomes smaller than a predefined value.

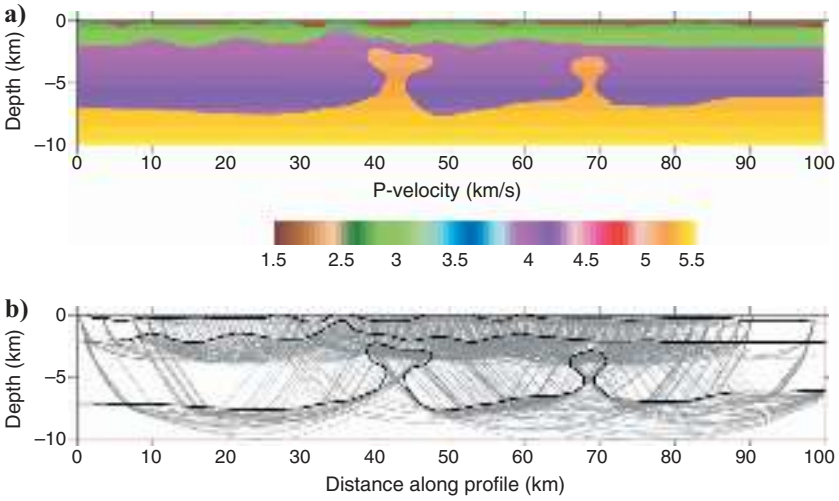

Figure 2. General setup of the Salt model. (a) Velocity distribution in the true model. (b) Raypaths used in the modeling. In this plot, only one-tenth of the total number of rays are shown.

The feasibility of the algorithm is illustrated based on the synthetic Mount model in Figure 1. Figure 1b presents examples of two rays constructed using this algorithm. Thin black lines show the paths in 20 iterations used to construct the final ray (red lines). A simple cosine-shaped line is gradually transformed into a complex shaped path that tends to pass through high-velocity patterns and avoids slow areas. The rays between sources and receivers located on the surface that were used in the experiment are shown in Figure 1c. The rays mostly travel inside high-velocity layers, and in some cases they are similar to the head waves. The low-velocity areas are generally poorly covered by the rays. Raypaths for the Salt model are presented in Figure 2b.

The bending method provides these ray solutions for a fixed calculation time that remains stable for any source-receiver pair. In a complex model such as Mount, an alternative shooting method would not be able to ensure a stable solution. It is important that our bending algorithm works for any parameterization of the velocity model (e.g., with regular or irregular grids, polygons, gradient layers). It has no limitations to the velocity values and shapes of features in the model.

In addition to the algorithm used in the PROFIT code, several other modifications of bending codes were designed for different models, e.g., 3D tracing (Koulakov, 2009a), anisotropic 2D and 3D models (e.g., Koulakov et al., 2009a), and 2D models with sharp interfaces of complex shape. The latter is described briefly in Appendix B and compared with the shooting code. We show that the bending code always provides the solution corresponding to the first arrival (global minimum), but the shooting solution may correspond to other branches of caustics (local minima that correspond to larger times than provided by bending). The misidentification of phases in shooting can result in significant errors and artifacts in further processing.

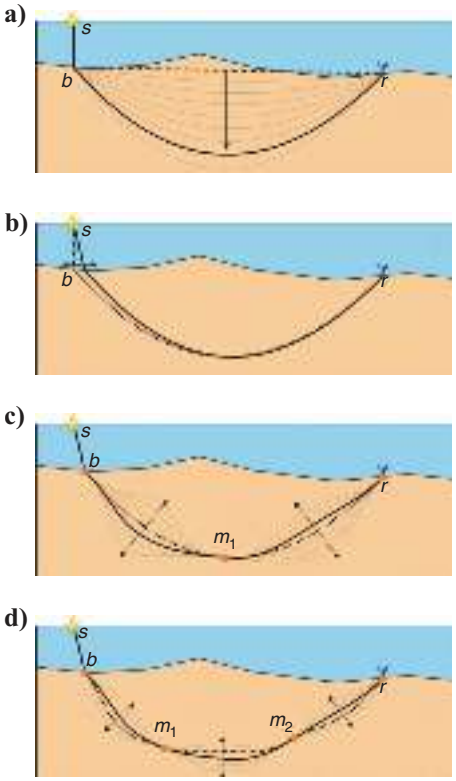

Figure 3. Sketch for explaining the principle of our version of the bending algorithm. Refer to the text for explanation of the views.

An alternative method of kinematic forward modeling is solving the eikonal equation. When the observation has few sources and many receivers (land profiles) or many sources and few receivers (marine profiles), such an approach may appear quite effective. However, for modeling first-order interfaces and strong heterogeneities, the eikonal equation requires a rather fine mesh, increasing computing time. In addition, to perform the tomographic inversion, we need the rays; the eikonal approach requires an additional step of transforming wavefronts to rays, which may create unexpected problems.

Parameterization

We define the 2D velocity distribution using node parameterization, developed for 3D passive tomographic inversion using the LOTOS code (Koulakov et al., 2007; Koulakov, 2009a). The values of velocity anomalies are interpolated bilinearly between the nodes. The nodes are defined in a set of vertical lines with a fixed, predefined spacing. Along each line, we compute the values of the ray density (normalized total length of rays in a unit volume). The nodes are then distributed according to the ray density. To avoid excessive node fluctuations, we define the minimal spacing between the nodes in the vertical direction. In areas with lower ray density, the distance between nodes is larger. No nodes are defined in areas where the ray density is less than a predefined value (e.g., 0.1 of ray density with respect to the average value). The grid nodes are installed only in the first iteration according to the ray distribution traced in the starting model. During later iterations, velocity variations are updated based on the same nodes.

Figure 4 presents examples of grid construction for the Mount, Salt, and Sea models. The Salt and Sea cases correspond to wide-angle observations for which the node spacing in the horizontal and vertical directions is not equivalent (e.g., 2 and 0.3 km in Sea) because we expect a different vertical and horizontal resolution.

By linking the node distribution to ray density, the grid may be adapted specifically to any data set, accounting for the distinct variation in ray density. Ray distribution and density are unique features in every refraction study, depending on the instrument layout and on the composition and geometry of the subsurface. This requires a nonuniform grid with variable grid sizes dependent on the ray distribution and density. Installing a nonuniform grid as a function of ray coverage represents a novel approach that is not implemented in existing noncommercial algorithms.

In the PROFIT code, the grid sizes are smaller than the minimal resolved size of anomalies, which can be estimated from synthetic modeling (e.g., checkerboard). In this case, the resolution of the model is controlled by the damping value and the model is grid independent. Changing the grid configuration does not significantly affect the resulting model. Appendix C provides an example of inversions using two significantly different grids for the Sea data set; the images are practically identical.

Matrix calculation and inversion

The first derivative matrix is calculated using the raypaths computed based on the ray tracing in the 2D model. Each element of the matrix $A_{ij} = \partial t_i / \partial V_j$ is equal to the time deviation along the ith ray resulting from a unit velocity perturbation in the jth node. The elements of the matrix are computed numerically.

The inversion of the overdetermined **A** matrix with a data vector perturbed by noise is unstable a priori. Therefore, this inversion should be regularized (e.g., Nolet, 1987) by adding two matrix blocks:

$$\begin{pmatrix} \mathbf{A} & \\ AM & \mathbf{I} \\ SM & \mathbf{C} \end{pmatrix} dV = \begin{pmatrix} dT \\ 0 \\ 0 \end{pmatrix},$$

where **A** is the main matrix of first derivatives, dT is the data vector, **I** is the diagonal identity matrix (with only one element in each line) that controls the amplitude of the solution, and **C** is the matrix block that controls smoothing of the solution. Each line of this block contains two nonzero elements 1 and -1 that correspond to all combinations of neighboring nodes. Changing the values of amplitude damping AM and smoothing damping SM controls the amplitudes and smoothness of the derived anomalies. Inverting the entire sparse **A** matrix is performed using an iterative LSQR algorithm (Paige and Saunders, 1982; Van der Sluis and van der Vorst, 1987).

The optimum values of AM and SM depend on several factors.

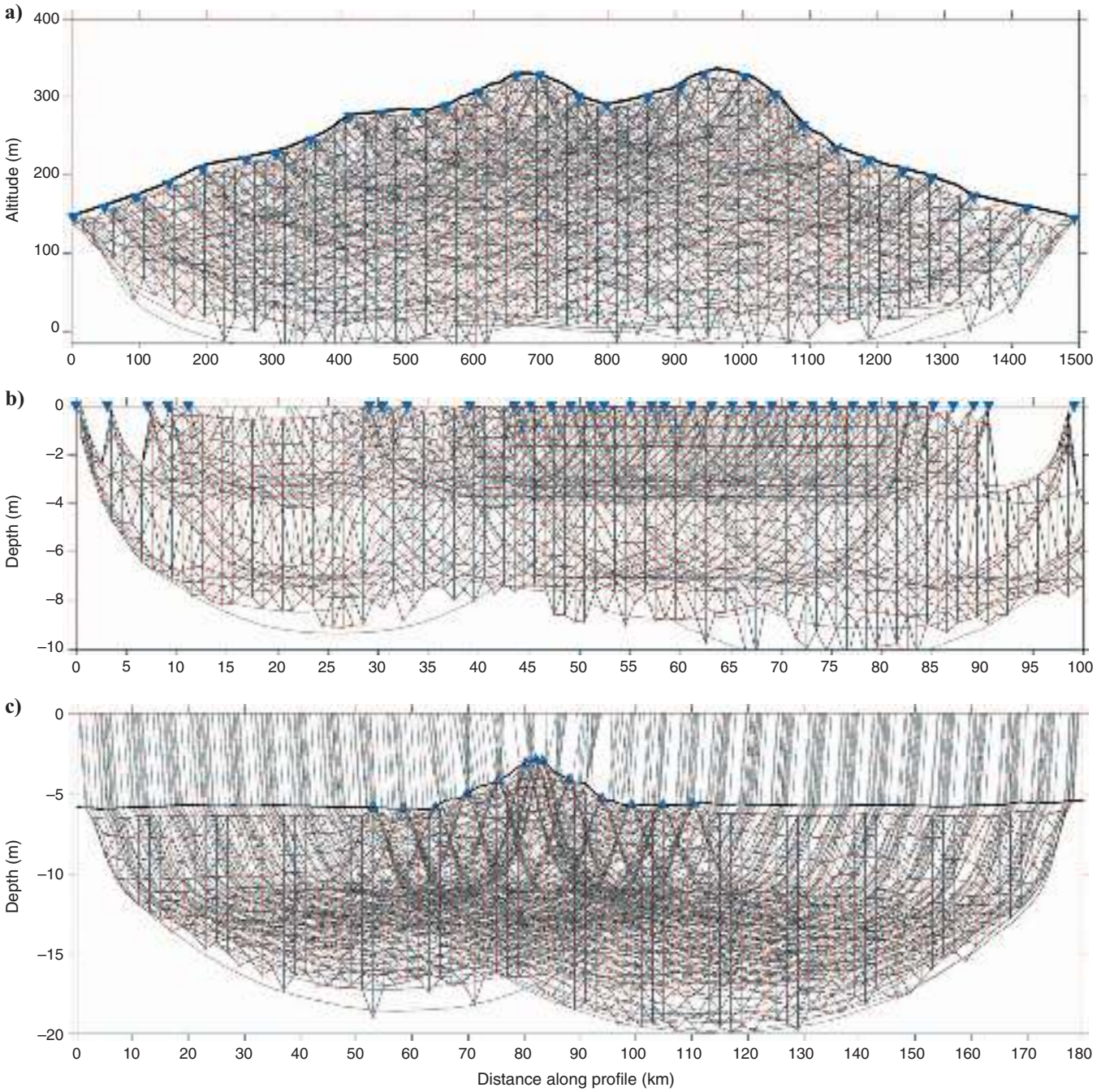

Figure 4. Raypaths in starting models (gray lines) and parameterization grids for the Mount, Salt, and Sea data sets. Nodes are indicated by red dots; thin black lines are links between the nodes used for smoothing. (a, b) The blue inverted triangles are the sources; in (c), the blue triangles are the stations on the sea bottom.

For example, when increasing the data amount, the damping parameters should be increased; in the case of increasing the numbers of nodes from smaller spacing, the damping should be decreased. In the case of larger noise levels in the data, damping should be stronger to stabilize the solution. The process of finding the damping coefficients is not formalized yet. Some authors use so-called L-curves or trade-off curves (TOCs), which show the amplitude of the solution versus rms of residuals for different damping values (e.g., Eberhart-Phillips, 1986). They propose that the value in the corner point of the L-shaped curve corresponds to the optimal damping. However, Koulakov (2009a) provides several arguments why TOCs are inappropriate for estimating damping in an iterative inversion. The most obvious argument is that in most studies (if not all), the TOC is computed in the first iteration and it does not know how many iterations will be performed. However, the same amplitude of the solution can be obtained for an underdamped inversion in one iteration and an overdamped inversion in several iterations. Furthermore, Koulakov (2009a) shows in synthetic examples that damping estimated with TOC is inadequate and does not provide the best reconstruction quality. Therefore, we strongly believe that TOC analysis should not be used in tomography.

An alternative method for determining the optimal values of damping parameters is synthetic modeling. Using realistic configurations of rays, it is possible to tune the smoothing and amplitude damping parameters to achieve optimal similarity between the synthetic and resolved patterns. These parameters can then be used to invert the observed data with the corresponding ray configuration.

The velocity anomalies obtained after inversion are recomputed in a regular grid and added to the velocity model obtained during the previous iteration. Regular representation of the velocity field is more convenient for performing the ray tracing in the next iteration.

SYNTHETIC DATA PROCESSING (MOUNT AND SALT DATA SETS)

Creating the synthetic data

The PROFIT code provides several different options for defining velocity models. In all cases, the velocity is a superposition of a basic velocity distribution and velocity anomalies. The basic velocity can be defined in different ways: 1D models, velocity values in a regular grid, linear velocity distributions between interfaces. For velocity anomalies, several options exist (e.g., checkerboard or anomalies inside polygons). Based on this algorithm, we have created two synthetic models that represent different realistic situations to illustrate the working ability of FM&TI.

The Mount model (Figure 1a) simulates a 1500-m-long profile that passes through a hill with an approximate relative elevation of 170 m. In this case, we model different geologic features such as magmatic batholith and sill-shaped intrusions, layered rocks with strongly varying properties, faults, and sediments. In the fault area, we produce a low-velocity anomaly that represents the fractured zone. Around the intrusions, we define a metamorphic zone with higher velocities. The basic velocity is defined inside several areas separated by polygon curves. Inside some of these polygons (high-velocity intrusions), the velocity distribution with a vertical gradient is fixed; in other polygons (sedimentary layers), velocity is constant. Additional velocity variations (such as the high-velocity zone around intrusions of lower velocities in the fault zone) are defined as velocity anomalies inside polygon areas. This model is presumably too complicated to be resolved by a detailed tomographic approach. It is designed to check the capacity and realistic limitations of the algorithms.

We consider a realistic distribution of the observation schemes that includes 30 sources and 120 receivers installed on the surface of the hill. The rays with distances of more than 1000 m between sources and receivers are not considered. In this case, 3222 rays are used. Synthetic times are calculated using the bending algorithm of ray tracing. This is the same ray tracer used for the inversion, except with a much finer integration step along the raypaths, which is required to model small-scale and sharp velocity features adequately. Some rays for this data set are shown in Figure 1c. Note that these raypaths differ considerably from those derived in the starting model (Figure 4a). Even after an iterative inversion, the paths remain rather far from the true ones. This causes a systematic error, resulting from the nonlinearity of the inversion. The traveltimes and the model are available online (Koulakov, 2009b) and can be used for testing forward-modeling and inversion codes.

The Salt model is shown in Figure 2a. In this model, we simulate two high-velocity salt domes (yellow-orange bodies) and a sedimentary layer of variable thickness (green and brown). The velocity distributions with fixed vertical velocity gradients are defined in four areas separated by three curves. The data set for this model is generated based on a distribution of sources and receivers in an experiment in the Pre-Caspian area (Kazakhstan). The main purpose of this experiment was to detect and locate salt domes, which represent a critical aspect in planned oil exploration in this area. The synthetic model was created using existing source-receiver pairs. The raypaths in the synthetic model are presented in Figure 2b. In total, 11,758 rays corresponding to 42 shots generate the Salt data set. As with the Mount data set, one person created the model and computed the synthetic data set; another person performed reconstruction with no knowledge about the model.

Reconstructing the Mount synthetic model

The Mount synthetic model (Figure 1a) was created by one person, and the reconstruction was performed blindly by another person in the same scheme used to process measured data in real experiments.

When inverting the observed data (computed in the true model), we performed a series of trials using different starting models and different sets of damping parameters (SM and AM). The intermediate results of this search are presented in Appendix C. The best starting velocity model, which provides the minimal rms of residuals, is shown in Figure 5a. Note that parameterization of the starting model differed from that used for defining the synthetic model. In this model, constant velocity values are defined in three polygon lines (the first coincides with the profile relief, the second is an intermediate boundary, and the lowest is the horizontal line at $z = -20$ m). For fixed x along the vertical direction, we define a constant velocity gradient between these lines. Inversion results with $SM = 40$ and $AM = 30$ are presented in Figure 5b.

Now we can compare the inversion results in Figure 5b with the true model in Figure 1a. The brown sedimentary layer is resolved robustly. Velocity values and layer thickness are reconstructed correctly. The high-velocity intrusion bodies are reconstructed generally in the appropriate locations. The upper part of the left intrusion is resolved correctly in shape and amplitude. However, the lower part of this intrusion is strongly smeared horizontally, and the velocities in

this part are much lower than in the true model. As for the right intrusion, the inversion does not provide robust information about the shape of this pattern. The reconstructed body is much larger than the true intrusion. The horizontal high-velocity sills alternating with lower-velocity sedimentary layers are not resolved.

The inversion does not provide full information about the layered structure of sediments outside the magmatic bodies. However, some of the relevant patterns can be resolved. On the left side, between 150 and 350 m along the profile just below the green sedimentary layer, we observe a higher-velocity violet layer that overlies a lower-velocity blue layer. Between 800 and 1000 m, we correctly detect two inclined high-velocity layers. A thin high-velocity layer just below the right summit of the mount at about 1000 m of the profile is also visible. The other layers are not clearly detected in the inversion results.

Working blindly, we have tried to reconstruct a probabilistic synthetic model to reproduce the tomogram of the true data set inversion. To construct a probabilistic model, we cannot provide a formal algorithm that unambiguously leads to the best solution. In each concrete situation, finding a model might have some particular features. However, we have a general recipe. First, we digitize the shapes of the main patterns retrieved from the observed data inversion and create the synthetic model based on these shapes and retrieved velocities. After performing the first reconstruction using synthetic data, we can see that the velocities in some areas are too low or too high compared to the results of the observed data inversion. In this case, we correct the synthetic model in the corresponding parts and repeat the synthetic reconstruction.

Numerous different synthetic models were checked (see Appendix C). The final synthetic model that provides the best reconstruction is shown in Figure 6. However, an ideal fit of reconstructed observed and synthetic models (Figures 5b and 6b) was not achieved because of strong nonlinear effects. For example, to model a low velocity centered at $x = 850$ m and $y = 100$ m, we tried to decrease the velocity in this part. However, the reconstructed model did not implement these changes, probably because the synthetic rays avoided this low-velocity anomaly.

Reconstructing the Salt synthetic model

Reconstruction of the Salt model started from finding the best 1D velocity model, which was estimated after several trials. The best model, which provides the minimal rms, is presented in Figure 7a. We also tested several different values of amplitude damping and smoothing. Various examples of reconstructions with different reference models and damping values are presented in Appendix C. The most robust model is derived for $SM = 0.5$ and $AM = 0.5$ (Figure 7b). This model resolves the main patterns of the original model. All variations of the uppermost sedimentary layer (brown) are reconstructed correctly. The dark blue layer in the reconstructed model repeats the shape of the basement (interface between violet and green layers). In particular, the clear thinning of the sedimentary cover at 35 km of the profile is resolved. The salt domes are mapped in correct locations; however, their sizes and amplitudes do not fully correspond to the original model.

As in the Mount case, a probabilistic model was constructed to estimate the shape of the salt domes without a priori knowledge about the true velocity distribution. The synthetic model (Figure 8a) was constructed after six trials using FM&TI (see Appendix C). The cor-

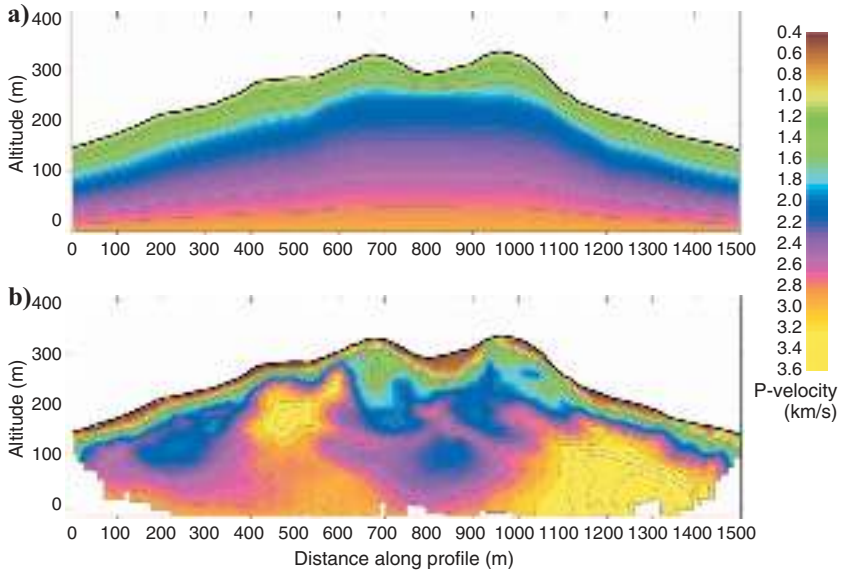

Figure 5. Result of inverting the Mount data set. (a) Starting velocity model. (b) Resulting model after 10 iterations of tomographic inversion. This result can be compared with the true model in Figure 1.

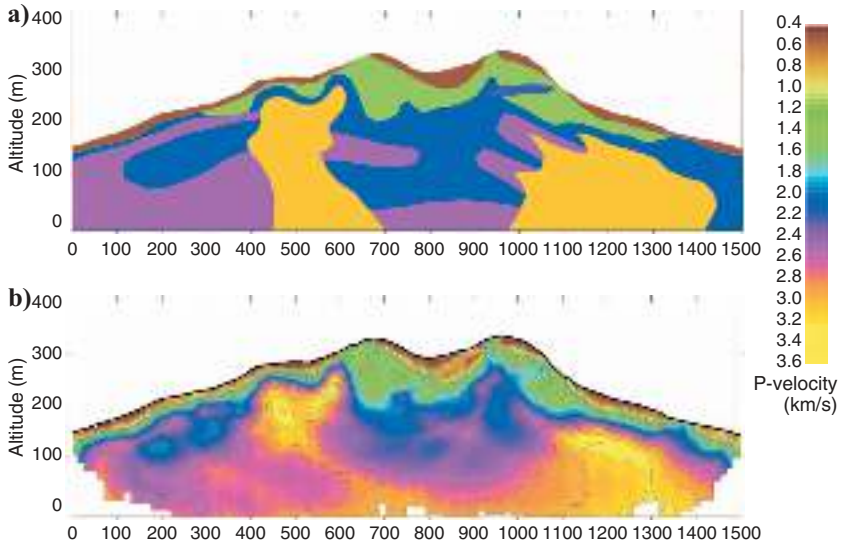

Figure 6. Blind synthetic modeling for finding a probabilistic model for the Mount data set. (a) The best synthetic model derived after several trials. (b) Result of inverting data computed by ray tracing in the model presented in (a).

responding inversion of synthetic traveltimes yields the tomogram in Figure 8b, which is strikingly similar to the observed data inversion in Figure 7b. A comparison of the retrieved synthetic model (Figure 8a) with the original model (Figure 2a) exemplifies the good fit of velocity values and shapes of the main patterns. FM&TI thus provides a structural model (Figure 8a) of geologic-tectonic features whose detailed extent would be difficult to define unambiguously based solely on the inversion result of the observed data (Figure 7b).

Processing real experiment data (Sea data set)

In this section, we consider a marine data set acquired in 1999 in the Musicians Seamount Province in the Pacific Ocean. Details of the experiment are presented in Appendix C. The seismic structure along this profile has been investigated by Kopp et al. (2003). They could clearly resolve the extrusive style of volcanism of the Musicians Seamounts, which is manifested in the crustal thickening. The coherent and uniform phase distribution and rather clear geologic structure along the profile are favorable for testing a new approach, and these are the main reasons why this data set was selected to demonstrate the working ability of FM&TI.

The observed traveltimes of the first arrivals of the Sea data set are shown by black dots in Figure 9. The data and picking accuracy are conservatively estimated as 0.03 s at near offsets and 0.12 s at the far-offset traces. There are more than 20,000 picks for this profile. We did not consider rays of less than 5 km offset between the bounce point and the receiver because they travel in water and do not penetrate the ground; thus, this offset range does not contain information about the earth's interior. After rejecting these rays, the number of rays reduced to 18,716.

Because of the high data density of the study, it is possible to use only a subset of the data to optimize the calculation speed without loss of the resulting resolution. In Appendix C, we present the inversion result based on three data sets consisting of (a) the entire data amount, (b) one-third of the original data, and (c) one-tenth of the original data. The results show almost identical reconstruction quality. Formally, this is because frequently distributed rays with similar paths correspond to almost identical matrix lines. Two close-to-linear dependent equations do not contain more relevant information for the inversion results than one equation. On the other hand, increasing the density of ocean-bottom stations will lead to a superior ray configuration, thus improving the resolution. For the main tomographic results presented in Figure 10, we used one-third of the entire data (6237 picks); when searching the optimal parameters and most realistic synthetic model, we used the one-tenth data set to perform several trials.

The starting model was parameterized as a 1D velocity model. We defined seismic velocities at distinct depth levels and presumed constant-velocity gradients between these levels. In most trials, we defined four levels; only two of them are within the depth range of the study area. The 1D model is adjusted manually by performing only the first iteration and comparing the rms of the residuals. For some of the 1D models, we performed a full inversion consisting of nine iterations. The optimum reference model obtained in this way for the Sea data set is presented in Table 1. In addition, we performed several inversions using various values for *SM* and *AM*, which are analyzed in Appendix C.

The main results of the observed and synthetic data inversion for the Sea data set are presented in Figure 10. All results are given in absolute velocities (left column) and relative anomalies (right column) with respect to the best 1D starting model presented in Table 1. Figure 10a and b presents results of observed data inversion. A positive velocity anomaly is recognized inside the seamount edifice, indicative of an extrusive magmatic origin atop preexisting oceanic crust (Kopp et al., 2003). At a depth of 11 km, we observe a low-velocity anomaly, which shifts the contour line of

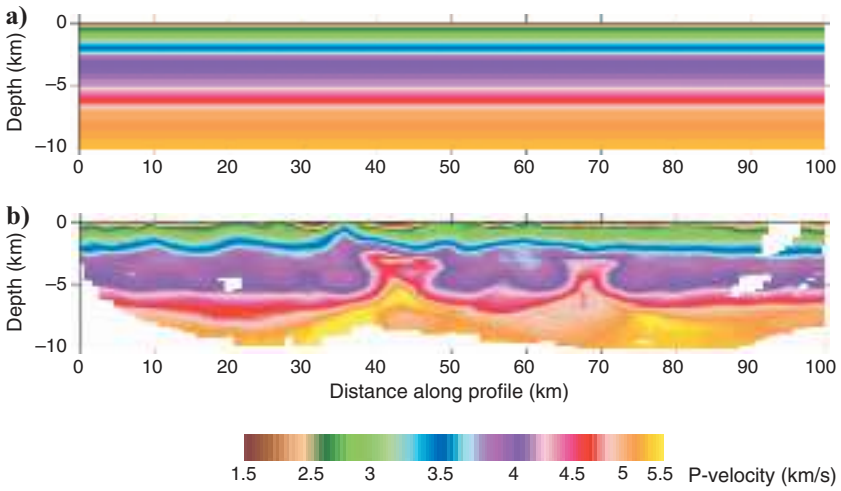

Figure 7. Result of inverting the Salt data set. (a) Starting velocity model. (b) Resulting model after 10 iterations of tomographic inversion. Compare this result with the true model in Figure 2a.

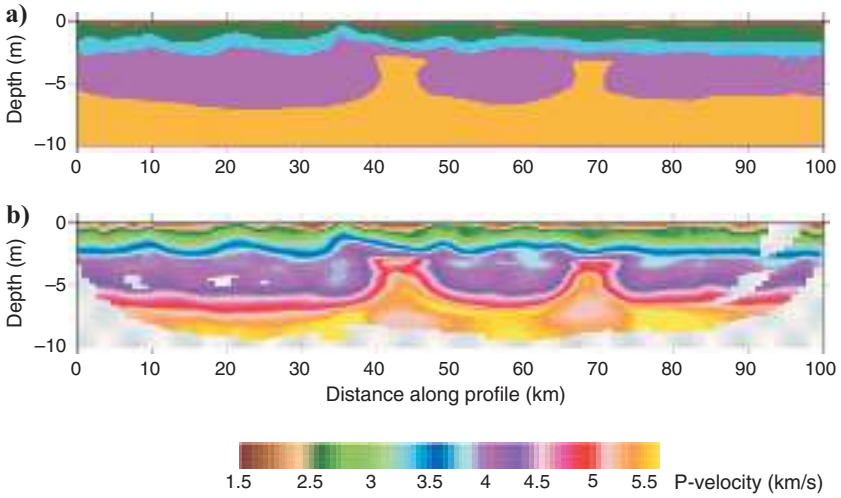

Figure 8. Result of synthetic modeling of the Salt data set. (a) Synthetic velocity model derived after several trials. Compare this result with the true model in Figure 2a. (b) Reconstruction results based on traveltimes computed in the synthetic model shown in (a). Compare this result with the observed data inversion in Figure 7b.

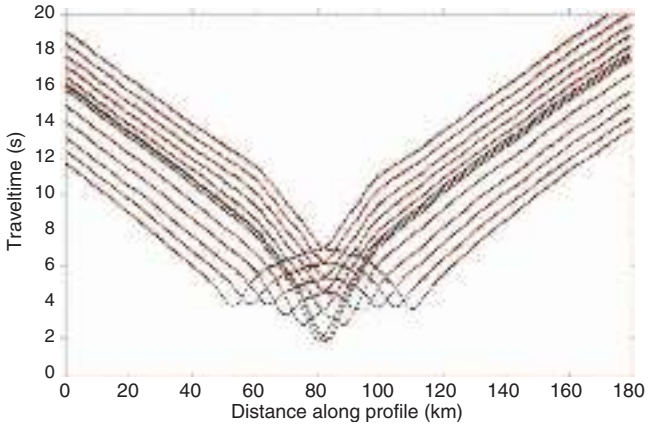

Figure 9. Traveltimes for the Sea data set. Black dots present the observed traveltimes. Blue dots are the traveltimes in the synthetic model (middle row, Figure 10). Red dots are the traveltimes in the resulting model after inverting the observed data (top row, Figure 11).

7.4 km/s from 10 km to approximately 12 km. This variation might be related to crustal thickening and a downbending of the Moho depth. Traveltimes of the derived velocity model after inversion are shown in Figure 9 with red dots.

An important test aimed at assessing the spatial resolution is the checkerboard test (see Appendix B). The reconstruction results show that most patterns discussed can be resolved robustly using the existing data.

A synthetic model, which was constrained after several trials, is presented in Figure 10c and d. The velocity distribution is defined in areas separated by layer boundaries. Furthermore, inside each velocity zone, we designate velocity anomalies with respect to the basic velocity distribution. The shapes of the anomalies are defined by polygons. The synthetic traveltimes are computed using the bending ray-tracing code. The reconstruction results based on these synthetic times are presented in Figure 10e and f. The reference model and all free parameters for tracing and inversion are identical with the observed data inversion.

Finding the best synthetic model is executed by trial and error. In Appendix C, we present examples of evolving synthetic models

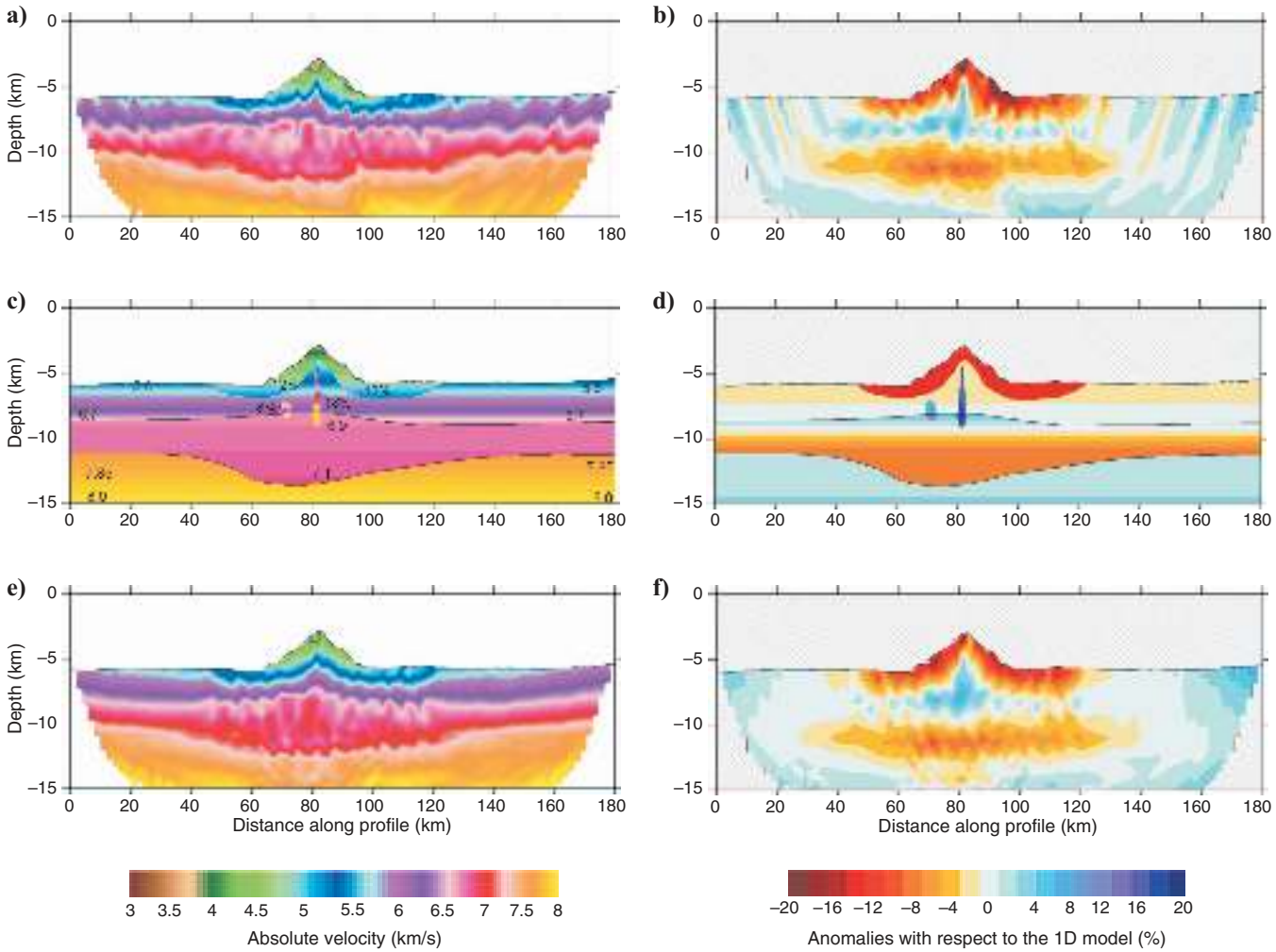

Figure 10. Results of observed data inversion and synthetic reconstruction HULA data set. (a, b) Results of tomographic inversion of observed data. (c, d) Synthetic model, constructed after several trials. (e, f) Result of the synthetic model reconstruction. In the left column, the models are presented in absolute velocity values. The right column presents relative perturbations with respect to the 1D starting model, which is identical for all three cases.

used to obtain the final synthetic model shown in Figure 10. These examples document how variations in Moho depth and of the channel contours inside the seamount affect velocities in the crust and other model parameters of the reconstruction results. Although tuning the model is rather time consuming, it is more stable and unique than in the case of classical forward modeling. Indeed, increasing the velocity or lowering the interface in one part of the synthetic model causes a velocity low in the resulting tomographic reconstruction of the same portion of the model.

We select the best model based on different criteria. The first criterion is the misfit between the observed and computed traveltimes during forward modeling in the synthetic model. The rms values of observed and synthetic traveltime differences $\|T_{obs} - T_{syn}\|$ of 12 different models are presented in Table 2. The second criterion is based on the difference between the velocity models obtained after the final inversion iteration for the observed data and the synthetic data, respectively. This value, indicated in Table 2 as $\|V_{real} - V_{syn}\|$, is computed on a regular grid for nodes where the solution exists. For the final synthetic model, we obtained good correlation between the inversion results of the observed and synthetic data. The traveltimes corresponding to the synthetic models are shown in Figure 9 with blue dots.

Table 1. Starting 1D velocity models used for the SEA data set. Depth z is given with respect to the seafloor.

z (km)	V (km/s)
2	3.8
6	5.7
11	7.5
20	7.9

Table 2. Values of time and model misfit in different synthetic models; $\|T_{obs} - T_{syn}\|$ indicates the rms between the observed and computed traveltimes in the synthetic model, and $\|V_{real} - V_{syn}\|$ is the difference between the resulting velocities after nine iterations of real and synthetic data inversions. Resulting images for the preferred models are presented in Figure 11.

Synthetic model	$\|T_{obs} - T_{syn}\|$	$\|V_{real} - V_{syn}\|$
1	0.0278	0.1841
2	0.0284	0.1600
3	0.0283	0.1488
4	0.0281	0.1288
5	0.0172	0.1108
6	0.0184	0.1119
7	0.0180	0.1170
8	0.0277	0.1187
9	0.206	0.1027
10	0.0181	0.0986
11	0.0148	0.0877
12	0.0283	0.1072

Figure 11 presents the variance-reduction curves for different synthetic models. For the preferred model, the curve of variance reduction (orange) is close to the values obtained by the observed data inversion (blue). The similarity of the variance-reduction curves in the observed and synthetic cases is another argument for the reliability of the proposed synthetic model.

DISCUSSION

Tomographic inversion usually biases the shapes and intensity of the real objects in the earth. Therefore, just reporting velocity values derived from tomographic inversion as a true representation of the earth's structure is not always adequate. FM&TI attempts to investigate the properties of the tomographic operator and derive estimates for the quantitative values of true structures. We propose that if two tomograms derived from inverting observed and synthetic data are identical, the known synthetic structure should be similar to the unknown structure in the real earth. At the same time, we admit that the inversion problem is fundamentally nonunique, and several different synthetic models may provide similar images on tomograms. Such nonuniqueness is shown, for example, for the Mount data set, which corresponds to a very complex velocity model. However, for simpler velocity distributions, especially when a priori information is available, the uncertainty caused by nonuniqueness of the inversion solution is strongly limited. This is illustrated by the Salt data set, for which we obtained a rather good fit.

The main motivation of using FM&TI is that grid-based inversions generally seek a smooth solution to fit observed traveltimes, failing to resolve sharp velocity contrasts. As stated, continuous velocity fields derived from tomographic inversion only represent a crude approximation to the natural velocity distribution, which originates from petrophysical material changes and distinct layer boundaries. In nature, the dominant velocity changes are related to first-order velocity changes at petrophysical interfaces. FM&TI, based on consecutively performing forward modeling and tomographic inversion, enables us to determine the most probable and realistic ve-

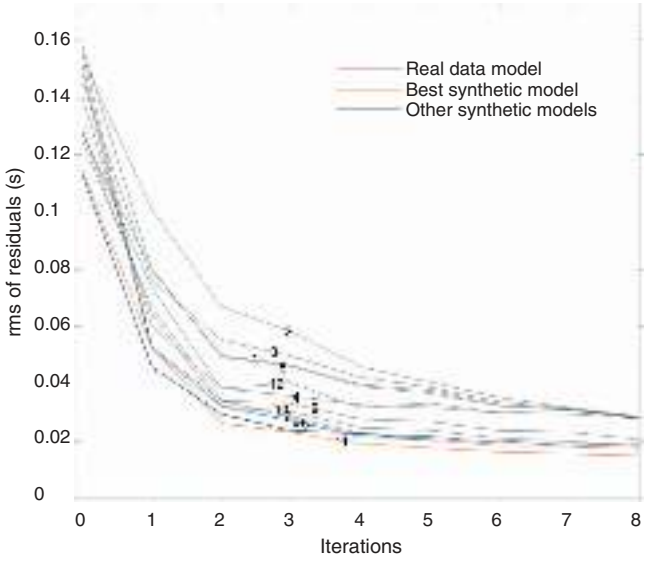

Figure 11. Variance reduction curves for different synthetic models and comparison with the real data model (blue line). The best synthetic model is represented by an orange line. The synthetic model numbers indicated in Table 2 are shown above the respective curves.

locity model. The difference of this approach compared to classical forward modeling is that in this case we compare the tomograms, not the traveltimes, which appear to be more robust and unambiguous.

At the same time, we can see with the Mount data set that a model which includes distinct vertical and lateral velocity changes linked to fine shapes of tectonic structures represents a very difficult object for reconstruction purposes. Nonlinear effects may bias the solution considerably, as seen in Figures 5 and 6. Between the intrusions, we could not achieve sufficient resemblance of the models because the velocity distribution in this area is probably controlled by smearing of the high-velocity intrusion bodies. Thus, changing velocity values in the model inside this area (e.g., adding a low-velocity body) did not improve the similarity of the images.

Despite these problems, FM&TI generally provides correct velocity values in the model. Comparing the models in Figures 1a and 6a, we can see that the main patterns in the upper part of the section (above 150-m altitude) are resolved correctly. Special caution, however, is required when interpreting deeper layers because the robustness of the reconstruction is much lower. The most important result is that even for such a complex model, the probabilistic synthetic model shown in Figure 6a is closer to the true model (Figure 1a) and contains more relevant information for geologic interpretation than the smooth result of tomographic inversion of measured data (Figure 5b).

Much more clearly, the positive effect of FM&TI is seen in the example with the Salt data set. The probabilistic synthetic model in Figure 8a correctly represents all patterns in the true model. Despite some differences in the shape of the salt domes and velocity values, this model represents the reality much better than a smooth result of tomographic inversion in Figure 7b.

For the Sea data set, we obtained some important geodynamic results. The tomographic inversion (Figure 10) supports the importance of extrusive volcanism in the Musicians Seamount Province, causing thickening. In addition, from the structural forward modeling, we were able to identify secondary intrusive processes, which added to the evolution of the volcanic elongated ridges (VERs). Whereas the velocity-depth distribution derived from the tomographic inversion provides a substantiated image of the general structure, the detailed anatomy of the volcanic ridges could be resolved only by the combined approach of tomographic forward and inverse modeling. Our new procedure obtained a realistic structural model, satisfying the observed traveltimes.

Performing the FM&TI technique provides the qualitative parameters of the velocity model. The synthetic model in Figure 10c and d consists of three layers separated by a midcrustal interface and the Moho. In the upper crust, we define a strong velocity gradient of 5.6–6.9 km/s for the depth interval of 6–9 km. In the lower crust, a decreased velocity gradient of 6.9–7.0 km/s for the depth interval of 9–13 km is applied. Beneath the Moho, we fix the velocity variation of 7.85–8 km/s for the depth interval of 12–15 km. Along the central portion of the profile beneath the seamount, the Moho depth increases from 11 km to approximately 13.5 km. Inside the seamount edifice, we define a 2–3-km-thick channel displaying a +18% velocity increase. We tested different values for the channel thickness and amplitudes and found that this configuration provides the most similar reconstruction model. To the north of the channel, we specify another positive anomaly of 8% deviation. On the flanks of the seamount, we introduce a low-velocity anomaly of −12% amplitude.

The velocity distribution gained from the tomographic inversion reveals the macrostructure of the VERs and supports earlier investigations using tomographic inversion (Kopp et al., 2003). Crustal thickening is interpreted as an indication for the extrusive character of the volcanism forming the seamounts and ridges. Top loading of the volcanoes results in a flexural structure of the oceanic crust, causing a downbending of the Moho underneath the central volcano. The fine-scale structure, however, is only disclosed from combining tomographic forward and inverse modeling, e.g., the discernible high-velocity channel that extends from the lower crust into the seamount edifice (Figure 10c and d). This feature might be caused by secondary intrusive processes, which, though suggested by Kopp et al. (2003), could not be resolved from tomographic inversion alone.

Finally, the role of nonuniqueness for the case of the Sea data set needs to be addressed. The same reconstructed anomalies can result from velocity anomalies or interface variations. For example, the low-velocity anomaly at 11 km derived in the observed data result is reproduced by a Moho decrease from 11 km down to 13.5 km in the synthetic model. The same low-velocity anomaly in the reconstruction model could be obtained by applying a smaller Moho deviation (e.g., down to 12 km) and a coeval greater-velocity step at the Moho. However, we cannot significantly change the velocity beneath the Moho because long rays are very sensitive to this value and its variation would cause increasing residuals for such rays. Thus, the contrast may be increased by a velocity decrease at the base of the crust. Nevertheless, we cannot change the velocity at the base of the crust because the value of 6.8 km/s at 8 km is fixed to model the traveltimes of shallow rays. Decreasing the velocity value in the crust at 13 km would cause a negative velocity gradient, which is unlikely. Although the theoretical problem of nonuniqueness exists in forward/inverse modeling, in practice we have little freedom in creating geologically reasonable models based on existing a priori information that satisfy the data. To reduce the ambiguity related to nonuniqueness, it is helpful to incorporate a priori information if available.

The practical value of any study is validated when many specialists in a given field further test data and compare results. We encourage colleagues to test other forward-modeling and inversion-based code results on our data sets. The synthetic velocities for the Mount and Salt models, the computed traveltimes, and detailed descriptions are available online of the Web site of the PROFIT code (Koulakov, 2009b).

CONCLUSIONS

Using three different data sets, we have demonstrated the capability of FM&TI to provide probabilistic velocity structures that may include smooth velocity variations as well as first-order interfaces. A new code minimizes computing time by applying a new algorithm of the bending method of ray tracing. In contrast to the graph methods of pseudobending commonly used, our bending method does not require a grid; it allows any velocity parameterization (with cells or nodes, with polygons or layers, with some analytical laws). As a result, it provides more accurate solutions in significantly shorter calculation time.

The FM&TI approach is novel for active source tomography. We have presented results of its application for two synthetic and one measured data set corresponding to velocity models of different complexity and scales. The probabilistic synthetic models in all cases are closer to the true velocity distributions than continuous velocity models derived from tomographic inversion of observed data. At

the same time, the solution based on FM&TI seems to be advantageous compared to classical forward modeling based on ray tracing of refracted rays. It allows updating velocity based on analysis of tomograms, not traveltimes, as in the case of forward modeling. This provides more stable and unambiguous solutions for velocity distributions.

FM&TI allows one to construct a geologically reasonable synthetic model of the study area. This procedure is beneficial to the geologic-tectonic interpretation because it provides a structural model in addition to the continuous velocity field created by the tomography.

All of these features of FM&TI allow applying this approach in real experiments with different observation schemes and on various scales. We have shown an example of the Mount data set, which may be used as a template for engineering tasks such as planning tunnels or monitoring dams. The example with the Salt data set demonstrates that the approach can be of great use for exploring the shapes of highly contrasted bodies such as salt domes and intrusions. This could be very important when exploring for oil or ore. Future work will address successful examples of using this approach in other situations, from small-scale crosswell cases to deep seismic sounding profiles in subduction zones.

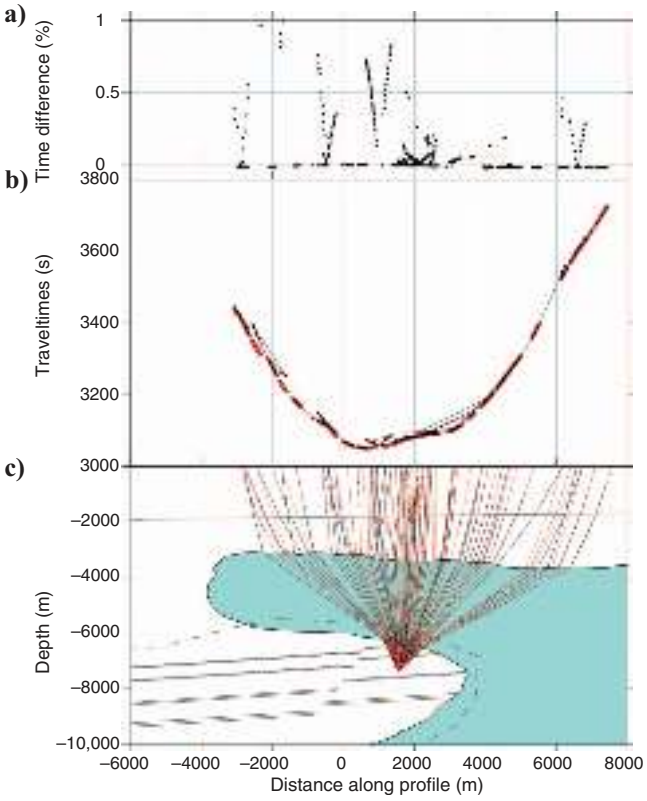

Figure A-1. Comparison of the results of tracing computed with shooting and bending algorithms. (a) Normalized difference between traveltimes computed by shooting and bending, $100\%*(T_{shooting} - T_{bending})/T_{bending}$. (b) Traveltimes computed by shooting (black dots) and bending (red dots). The data correspond to the step of ray shooting equal to 0.1°. (c) Raypaths computed by shooting (black) and bending (red). These rays correspond to the step of ray shooting equal to 1°.

ACKNOWLEDGMENTS

The refraction data were acquired by the *RV Sonne* in the 1998 Sea experiment (supported by the German Ministry of Finance and Education BMBF). I. Koulakov and T. Stupina were supported by the Russian Foundation for Basic Research (RFBR) (grant 08-05-00276) and the Helmholtz Society/RFBR Joint Research Project (09-05-91321-SIG). We thank A. Shulgin for fruitful discussions on seismic tomography. We are grateful to Associate Editor Sergio Chávez-Pérez, Børge Arntsen, and four anonymous reviewers for their rigorous and constructive criticism, which helped us to improve the paper.

APPENDIX A

VERSION OF THE BENDING RAY-TRACING CODE FOR MODELS WITH SHARP INTERFACES AND COMPARISON WITH THE SHOOTING METHOD OF RAY TRACING

The bending ray-tracing code used in PROFIT is rather stable and fast. However, we have designed other versions of the bending algorithms that are oriented to specific conditions of modeling and are used in other codes. One is created for modeling rays in complex 2D media with sharp interfaces of complex shape (e.g., salt domes). In this case, we start from a straight line and find the intersection points, with all interfaces having velocity contrasts larger than a predefined value. Then we move these points along the interfaces to achieve the minimum of traveltime. After finding a curve consisting of straight segments with nodes on the main interfaces, we continue iteratively bending the entire ray using the cosine approximation.

This algorithm has been tested using a realistic salt dome model (Figure A-1c). For this case, we made the comparison with the results obtained from the shooting algorithm. We used our version of a 2D one-point shooting code (ray traced from a fixed point with fixed starting direction) based on solving the ray differential equations. If rays met first-order interfaces, we used Snell's Law. For discontinuous and rough features in the velocity model, the shooting algorithm does not provide a stable solution of the two-point problem (ray tracing between two fixed points).

To compare the bending and shooting algorithms, we performed a series of shots with fixed steps of the starting angle (from $-20°$ to 40° with a step of 0.1°). Then we put the receivers in points of intersection of shooting rays with the upper surface and traced another ray for this source-receiver pair using the bending algorithm. The raypaths that resulted from the shooting and bending algorithms are shown in Figure A-1c. The traveltimes computed by shooting and bending methods are shown in Figure A-1b, and the normalized differences between shooting and bending times, $100\%\ (T_{shooting} - T_{bending})/T_{bending}$, are shown in Figure A-1a.

In most cases, the bending and shooting rays coincide with each other and the traveltimes are almost identical (difference is $<0.01\%$). However, in some cases, the raypaths and traveltimes computed by shooting and bending methods do not fit each other. In these cases, traveltimes of shooting rays are always larger than provided by bending. The reason for such discrepancies is that in a highly heterogeneous model, the traveltimes are usually perturbed by caustics when several rays with different traveltimes correspond to one offset. The bending method enables the first-arrival solution, but

the shooting may provide the ray corresponding to any caustics branches. Actually, when performing shooting, we cannot know whether the modeled ray corresponds to the primary of secondary branches. If the observed traveltimes are picked as the first arrivals and computed times correspond to secondary phases, this can result in considerable error of time residual computing when the shooting method is used. On the other hand, the incapacity of the bending tracing to model secondary phases might be a shortcoming of this method.

APPENDIX B

CHECKERBOARD RESOLUTION TEST

Besides reconstructing realistic shapes of anomalies, it is important to perform other synthetic tests to assess the resolution capacity of the resolved models. Here, we present the results of a traditional checkerboard test with different parameters of the periodic patterns.

The initial models for the tests (left column, Figure B-1) are represented by alternating positive and negative anomalies of $\pm 3\%$

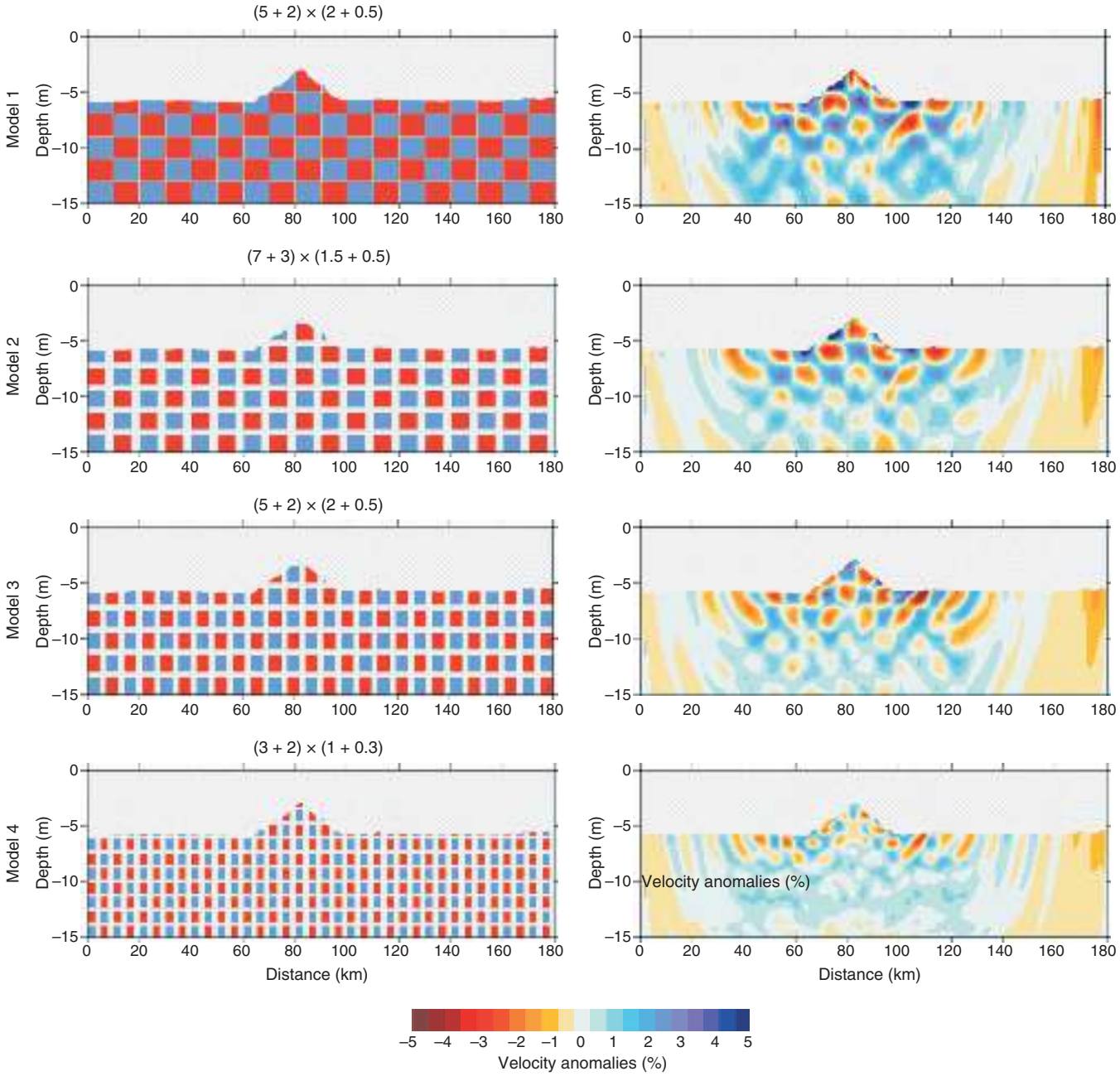

Figure B-1. Results of different checkerboard tests with different sizes of patterns (relative anomalies in percent). Left column presents the synthetic models. Numbers above each plot indicate pattern size. For model 3, $(5 + 2) \times (2 + 0.5)$ means that in the horizontal direction, the width of the anomaly is 5 km and tapering is 2 km; in the vertical direction, the height of the anomaly is 2 km and tapering is 0.5 km. In all models, the amplitude of synthetic anomalies is $\pm 3\%$. The right column shows reconstruction results after nine iterations.

amplitude. Horizontal and vertical sizes of each block are indicated above each plot. A variety of tests with different sizes of anomalies allows us to evaluate the resolving capacity of the algorithm based on the observed configuration of rays. Even the 3-km-wide and 1-km-deep patterns can be resolved in the center of the profile in the uppermost part. The larger anomalies are resolved in larger areas.

The traveltimes were computed using a 2D bending ray tracer. Rays computed in this way tend to travel through high-velocity anomalies. Therefore, the reconstruction in the first iteration is strongly biased to the positive value. After several iterations, the solution becomes more balanced regarding the amplitudes of positive and negative anomalies. Iteration 9 (right column, Figure B-1) shows a fairly stable reconstruction of most patterns in the area beneath the stations.

This test documents the importance of using a nonlinear iterative approach in tomographic inversions because the raypaths in the first and final iterations differ significantly.

APPENDIX C

EFFECT OF GRID CONFIGURATION ON TOMOGRAPHIC INVERSION RESULTS

In the text, we present the algorithm of grid construction for parameterizing a velocity model. We use fine grids with node spacing smaller than the size of minimal resolved patterns. Further decreasing the node spacing does not lead to any change in the resulting model. This is illustrated by an example with the sea data set (Figure C-1). The left column presents the results based on 2 km of horizon-

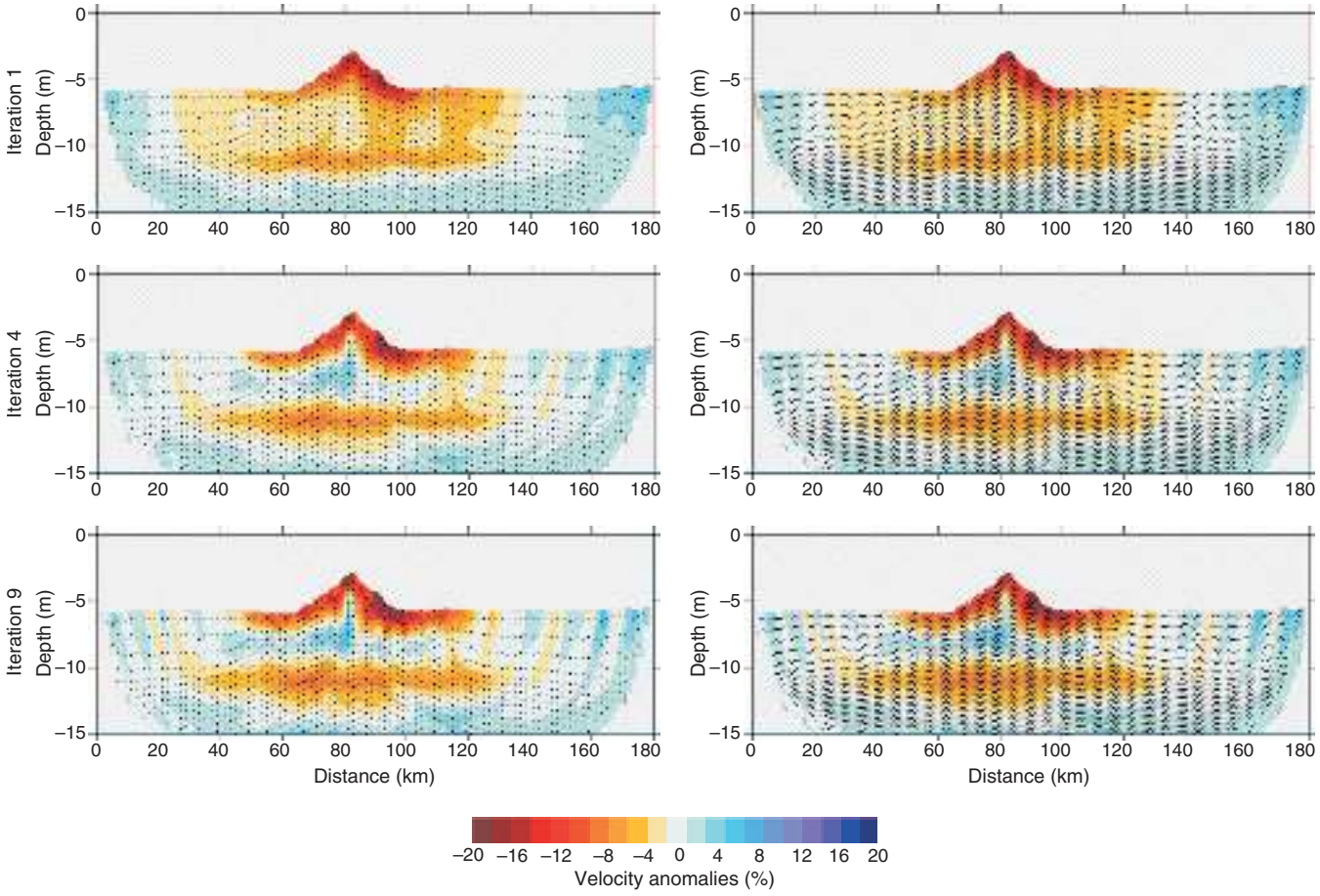

Figure C-1. Inversion results for the Sea data set based on two grids with different spacing. Velocity anomalies with respect to the starting model after iterations 1, 4, and 9 are presented for both cases. Left column: spacing $dx = 2$, $dy = 0.5$ km. Right column: spacing $dx = 0.5$, $dy = 0.1$ km.

tal spacing and 0.5 km of minimal vertical spacing (parameters used for the main results). In the right column, the corresponding parameters are 0.5 and 0.1 km. In all iterations, the solutions are very similar; if the grid spacing is less than the size of an expected anomaly, further decreasing the spacing will not affect the model.

Tuning starting model and free parameters

When processing any data set, we tested several different parameters to find the most appropriate ones. The most important parameters, which determine the solution, are starting-velocity distribution and damping (smoothing and amplitude regularization). Here, we present examples that show how these parameters affect the solution.

In the main text, we present the reconstruction results for the Mount data set. To obtain the results, we tested dozens of different starting and free parameters to find the most optimal ones. Figure C-2 illustrates two cases of using different starting models for the Mount data set. These are the inversion results after 10 iterations with the same free parameters used to compute the main model (Figure 6). Despite considerably different starting values, the final solutions are quite similar, especially in the upper part of the section. Figure C-3 presents the inversion results for different *SM* and *AM* values. The starting model is the same as for Figure 6. Finding the best-

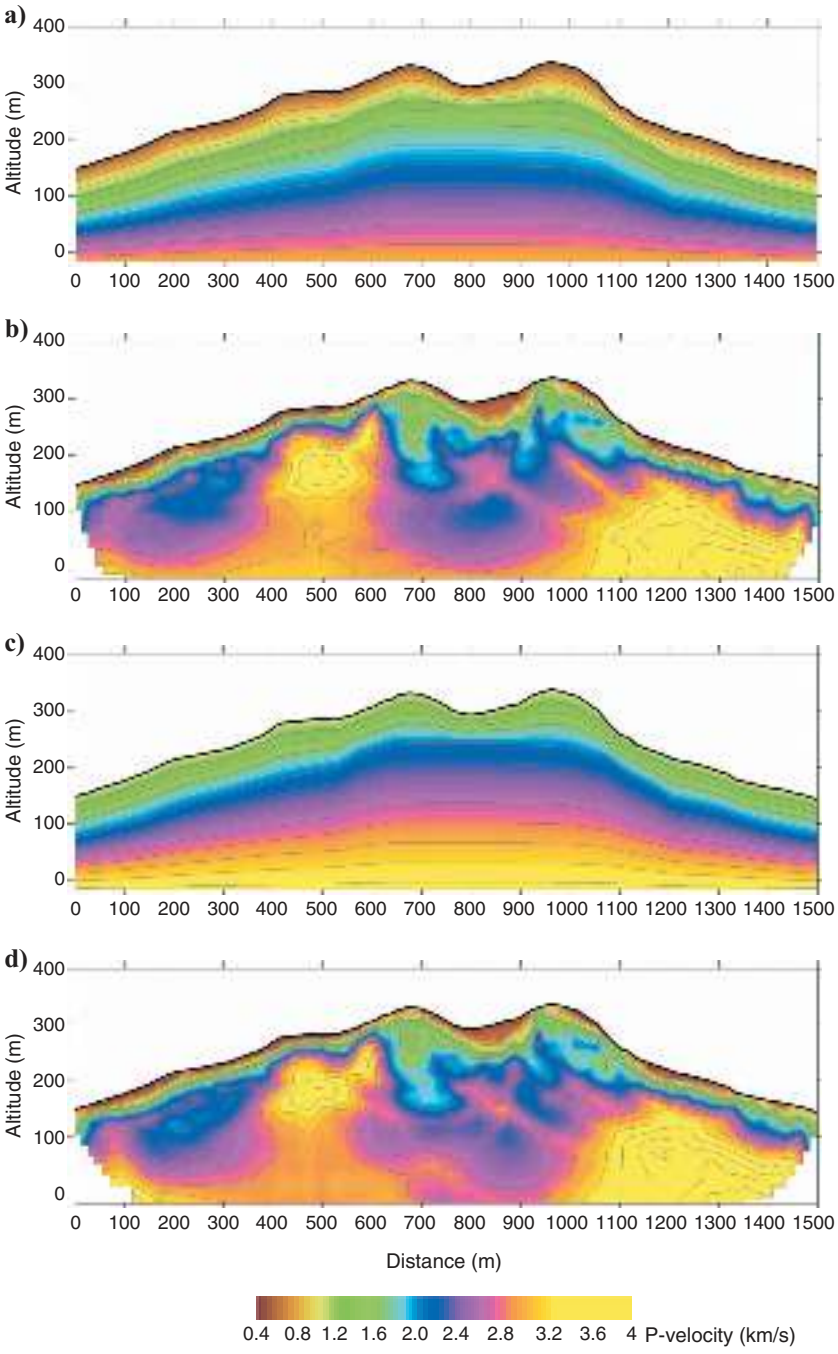

Figure C-2. Inversion results for the Mount data set based on two different starting models. (a) Model 1 starting-velocity distribution. (b) Inversion result for model 1. (c) Model 2 starting-velocity distributions. (d) Inversion result for model 2.

model is based on analyzing the rms of residuals. In Figure C-4, we graph variance reduction in 10 iterations for different starting models and SM/AM values.

For the Salt data set, Figure C-5 presents several examples of inversions with different SM and AM parameters. The best solution provides the minimal rms of residuals: $SM = 0.5$ and $AM = 0.5$.

For the sea data set, we only present the curves of variance reduction for different reference models and values of SM and AM (Figure C-6). For the models with weak damping, the solutions become unstable. For the overdamped solutions, the rms is also larger than in the optimal case.

The real marine experiment (sea data set)

The Sea real data set corresponds to a marine profile in the central Pacific near Musicians Ridge. The inactive Musicians Seamounts form coherent volcanic elongated ridges (VERs), which originated from hot-spot/ridge interaction. Their evolution is related to off-axis volcanism overlying partially melting asthenospheric flow channels linking the Euterpe hot spot and the Pacific-Farallon spreading center. The previously conducted tomographic inversion could clearly resolve the extrusive style of volcanism of the Musicians Seamounts, which is manifested in crustal thickening. This data set was

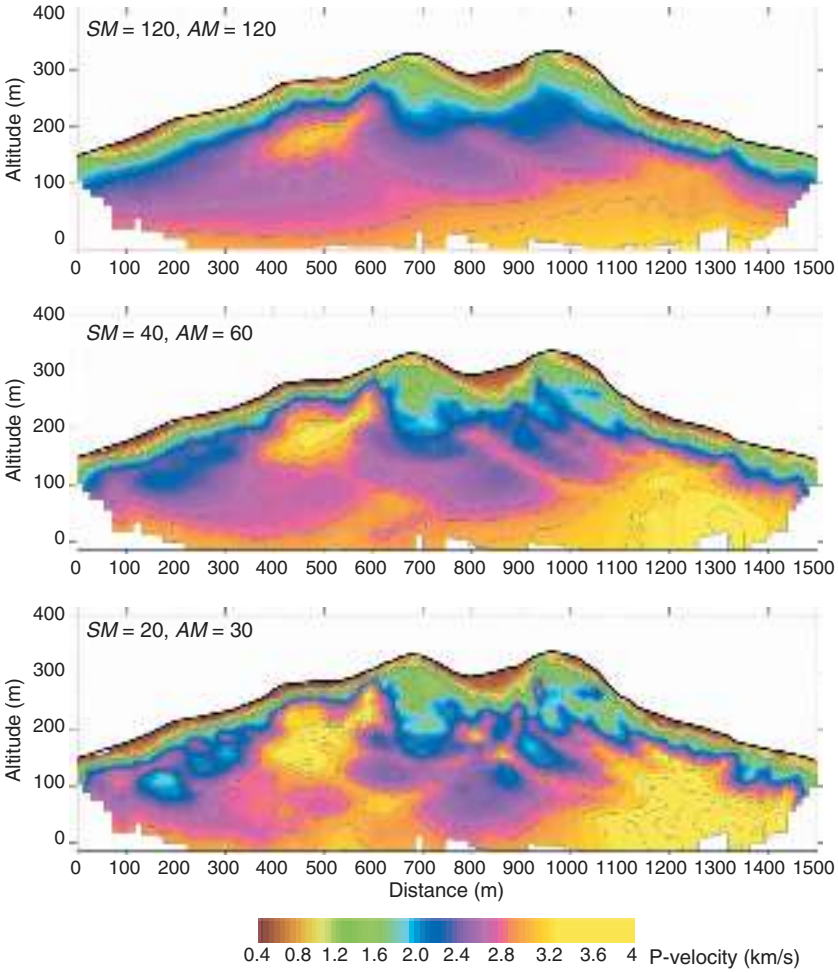

Figure C-3. Inversion results for the Mount data set, based on different values of smoothing (SM) and amplitude damping (AM).

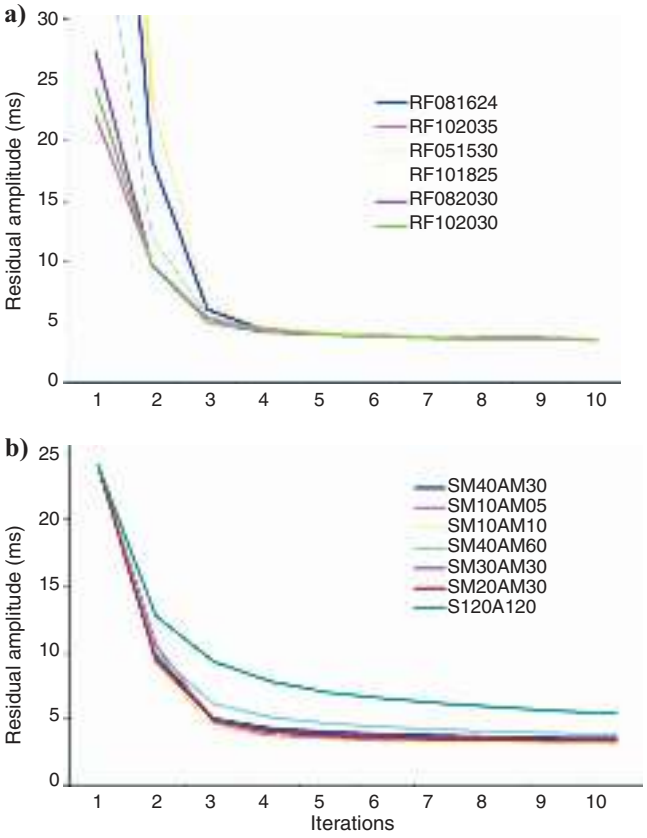

Figure C-4. Variance-reduction curves during iterative inversions based on (a) different starting models and (b) different *SM* and *AM* parameters.

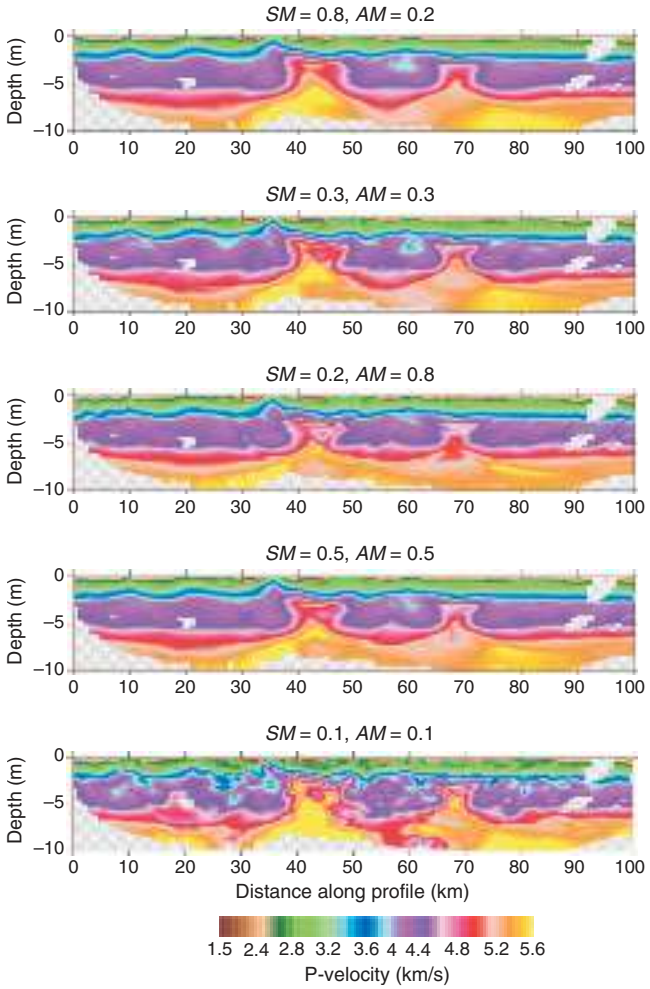

Figure C-5. Results of inversion for the Salt data set based on different values of smoothing (*SM*) and amplitude damping (*AM*).

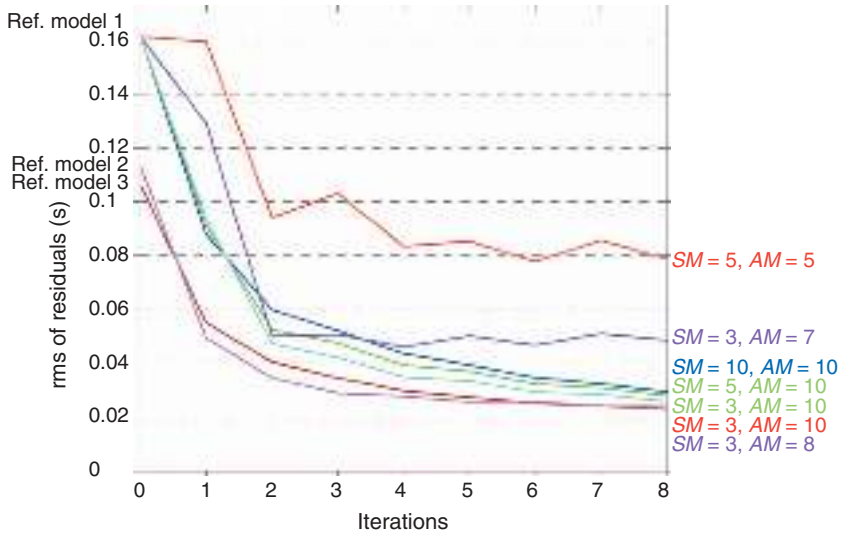

Figure C-6. Values of residual amplitudes after eight iterations for the Sea data set. The curves correspond to different values of *AM* and *SM*. Here, we consider three different reference models.

chosen because the coherent and uniform phase distribution in the seismic sections is favorable for testing a new code.

The tomographic inversion is applied to one of several active seismic refraction lines acquired in 1999 in the Musicians Seamount Province (Figure C-7). Thirteen IFM-GEOMAR ocean-bottom hydrophones (OBHs) (Flueh and Bialas, 1996) were deployed along the 180-km-long SO142 line 02, which crosses the Italian Ridge, expressed by an approximately 30-km-wide and 3-km-high bathymetric elevation. The 220-km-long SO 142 line 04 is covered with 12 OBHs. It crosses the Bach Ridge and covers several smaller and larger seamounts. The mean instrument spacing along both profiles is approximately 4 km. Two Bolt air guns with a total volume of 64 l served as the seismic source, with a shot interval of 60 s and an approximate shot spacing of 120 m at a speed of 4 knots.

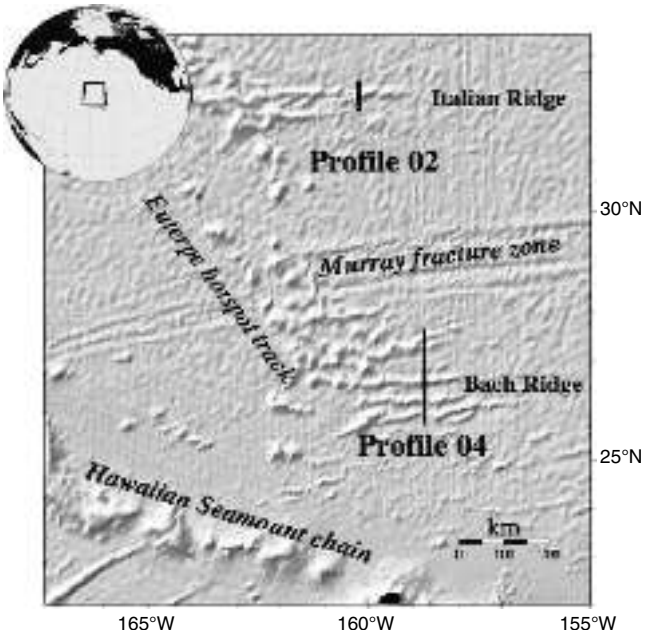

Figure C-7. Tectonic setting of the study area in the central Pacific. The Sea data set corresponds to profile 02. Volcanic features include hot-spot tracks, isolated seamounts, and VERs. The Musicians Seamount Province is bordered on the west by the Euterpe hot-spot track, to the north and south by the Italian and Bach Ridges, respectively; it terminates in the east at the former location of the Pacific-Farallon spreading center.

As is common for oceanic crustal structure investigations, the uniform tectonic structure of the study area yields excellent data quality, with phases recorded to offsets commonly exceeding 120 km and a high signal-to-noise ratio (S/N) (Figure 5). Only in the central part of line 4 do some stations display a lower S/N attenuating-phase coherency beyond 50–70 km offset. The oceanic crustal and upper mantle structure of the study area is fairly uniform, especially away from the volcanic edifices. The bathymetric elevations caused by the seamounts produce pronounced variations in apparent velocities. The generally smooth interval velocity distribution along the profiles, however, results in clearly differentiated upper and lower crustal refractions (Puc and Plc) as well as mantle refraction phases (Pn), which cover the entire shot-receiver offset range on most stations. The upper crustal refraction extends to offsets of about 25 km on most record sections, where it merges into the lower crustal arrival of gradually increasing velocities (Figure C-8). The mantle refraction appears between 50- and 60-km offset on both profiles, reaching maximum offsets of 140 km.

In the text, we discuss the problem of using data subsets instead of the entire data amount. Sources located close to each other can lead to almost linearly dependent equations in the inversion, which does not improve the solution. In Figure C-9, we consider three data subsets for the sea model that provide almost identical solutions, despite considerably different data amounts.

The best Mount model (Figure 9a) was constructed after performing six trials. Figure C-10 presents four of them. The model is too complicated, and the inversion appears to be very nonlinear. Changing velocities in the model does not necessarily cause a corresponding velocity change in the retrieved models. Some trials for a probabilistic model for the Salt data set are shown in Figure C-11. Analysis of the shapes of the retrieved anomalies in the trial-and-search process allows constructing realistic shapes of the salt domes in the synthetic model. Ten models used to construct a probabilistic model for the observed sea data set are presented in Figure C-12.

Figure C-8. Seismic wide-angle sections for OBH 11 of profile 02. Clear phases from the upper crust (Puc), lower crust (Plc), and mantle (Pn) are recognized to offsets of more than 100 km on several stations. Seafloor topography causes strong apparent velocities.

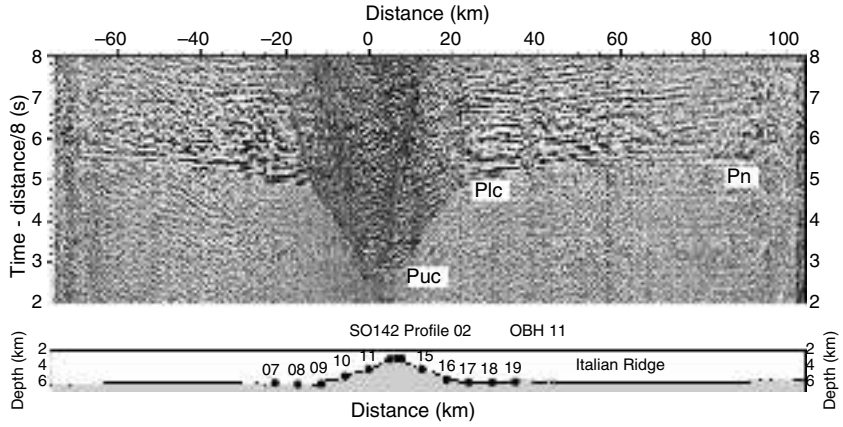

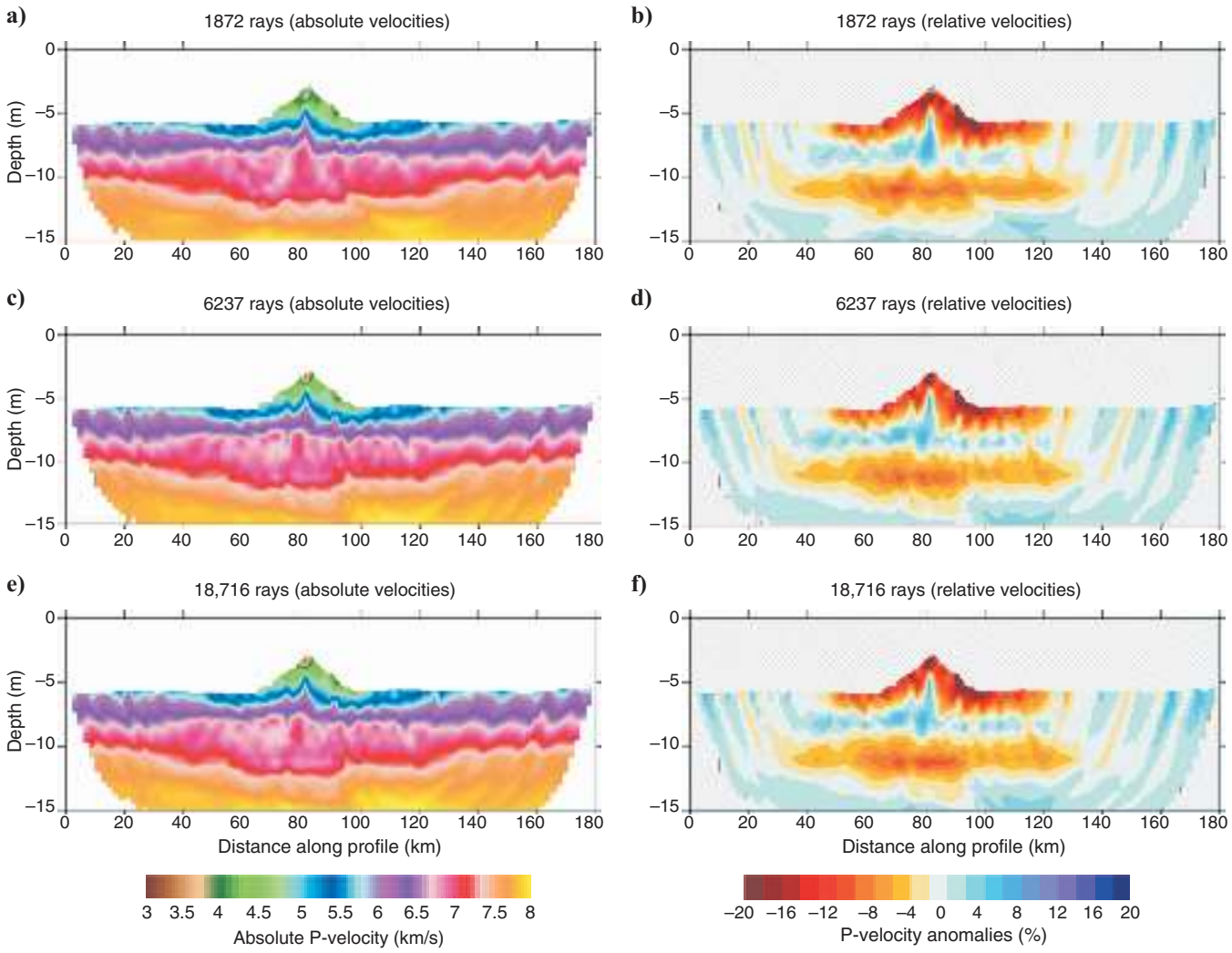

Figure C-9. Inversion results based on (a, b) one-tenth and (c, d) one-third data subsets and on (e, f) the entire data set. Numbers of rays for each case are indicated. Left column: absolute-velocity values. Right column: relative perturbations with respect to the 1D starting model, which is identical for all three cases.

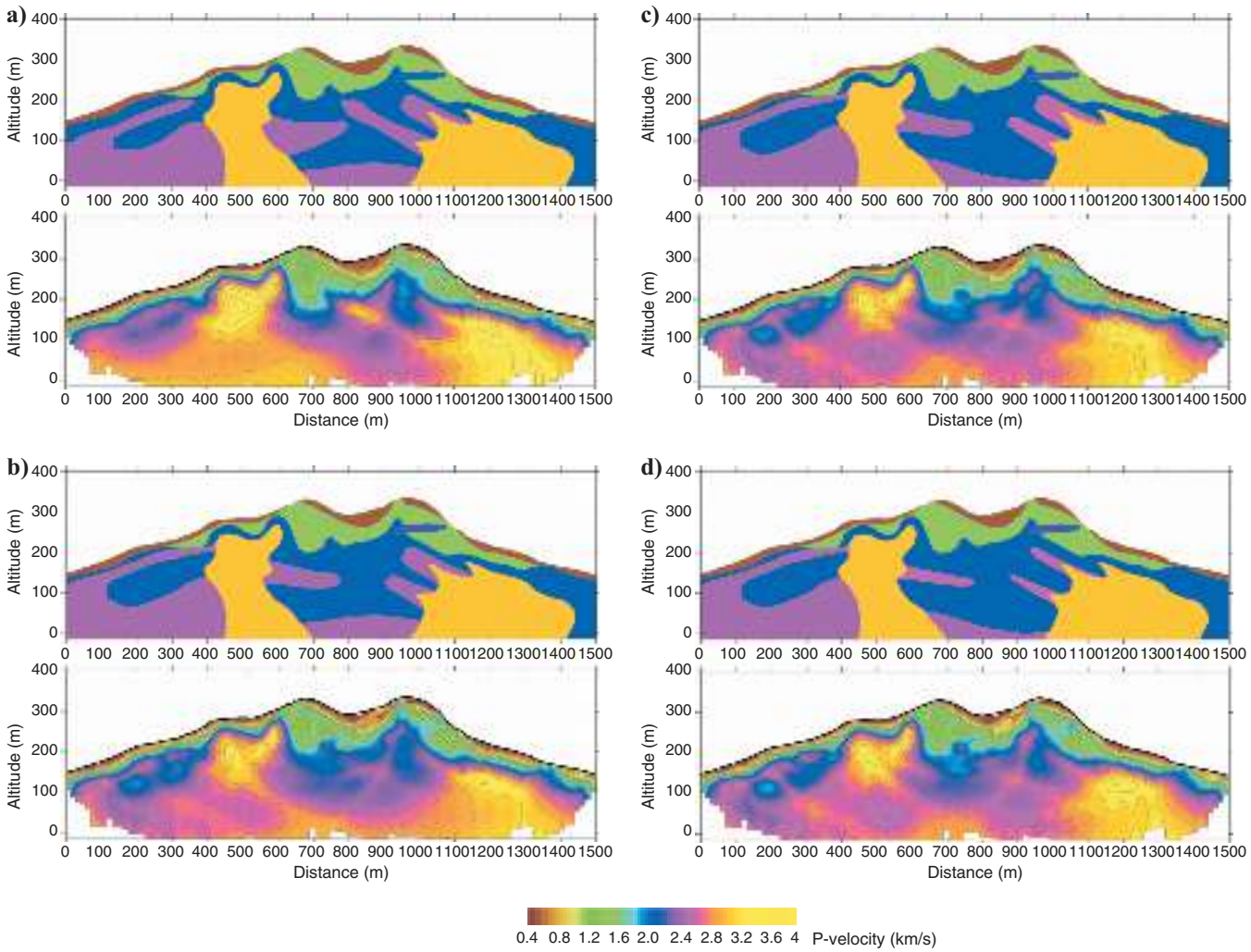

Figure C-10. Synthetic models (a) 1, (b) 2, (c) 3, and (d) 4, used to reproduce the results of observed data inversion for the Mount data set. In each pair, the upper plot is the synthetic model and the lower plot is the reconstruction result (after forward modeling and tomographic inversion).

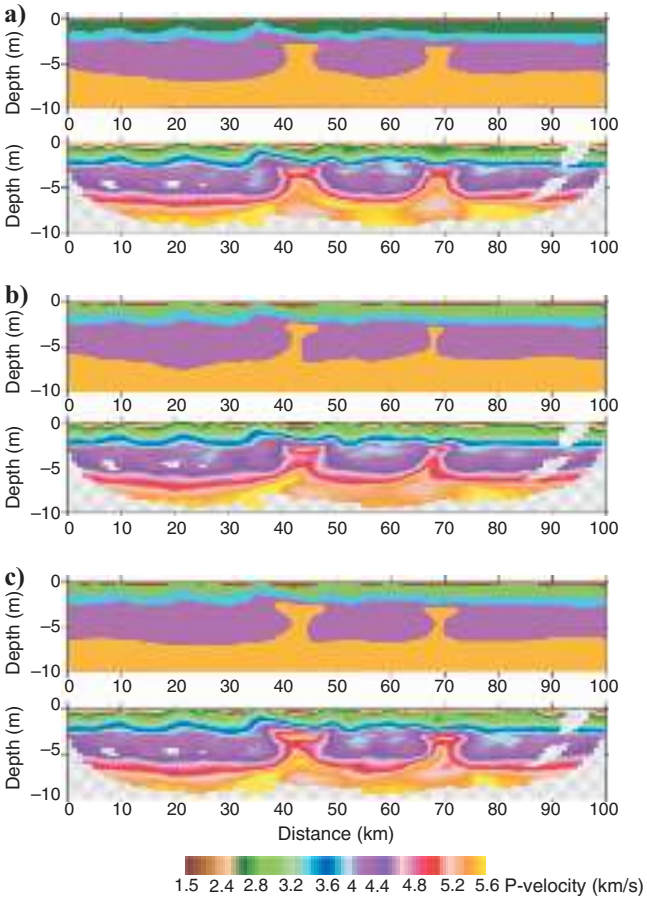

Figure C-11. Synthetic models (a) 1, (b) 2, and (c) 3, used to reproduce the results of observed data inversion for the Salt data set. In each pair, the upper plot is the synthetic model and the lower plot is the reconstruction result (after forward modeling and tomographic inversion).

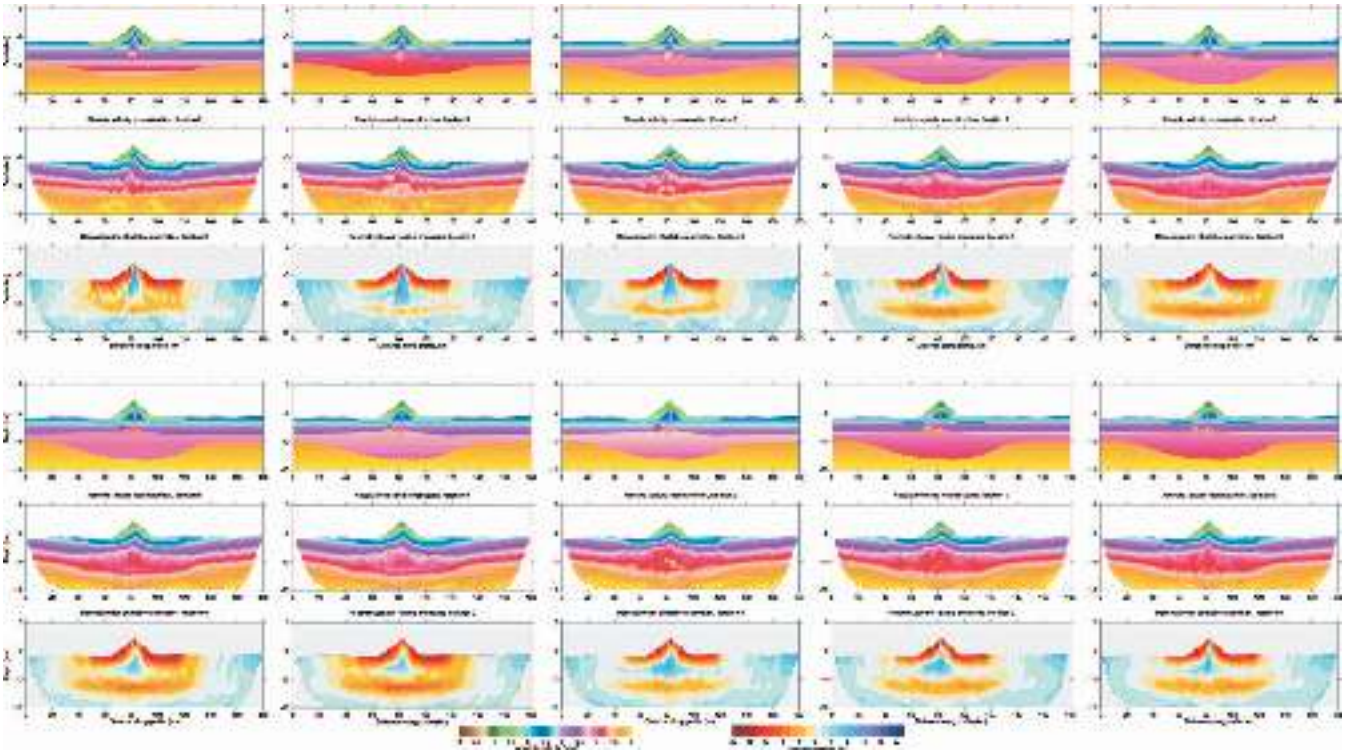

Figure C-12. Ten synthetic models for the Sea data set, used to reproduce the realistic model. Synthetic models are presented in rows 1 and 4. Results in absolute velocities are shown in rows 2 and 5. Resulting velocity anomalies with respect to the same 1D model are shown in rows 3 and 6.

REFERENCES

Eberhart-Phillips, D., 1986, Three-dimensional velocity structure in northern California Coast Ranges from inversion of local earthquake arrival times: Bulletin of the Seismological Society of America, **76**, 1025–1052.

Flueh, E. R., and J. Bialas, 1996, A digital, high data capacity ocean bottom recorder for seismic investigations: International Underwater Systems Design, **18**, no. 3, 18–20.

Freedman, A. P., and B. Parsons, 1986, SEASAT-derived gravity over the Musicians seamounts: Journal of Geophysical Research, **91**, 8325–8340.

Grechka, V., and G. A. McMechan, 1996, 3-D two-point ray tracing for heterogeneous, weakly transversely isotropic media: Geophysics, **61**, 1883–1894.

Hobro, J. W. D., S. C. Singh, and T. A. Minshull, 2003, Three-dimensional tomographic inversion of combined reflection and refraction seismic traveltime data: Geophysical Journal International, **152**, no. 1, 79–93.

Hole, J. A., 1992, Nonlinear high-resolution three-dimensional seismic travel time tomography: Journal of Geophysical Research, **97**, no. B5, 6553–6562.

Kopp, H., C. Kopp, J. Phipps Morgan, E. R. Flueh, W. Weinrebe, and W. J. Morgan, 2003, Fossil hot spot-ridge interaction in the Musicians seamount province: Geophysical investigations of hot spot volcanism at volcanic elongated ridges: Journal of Geophysical Research, **108**, doi: 10.1029/2002JB002015.

Korenaga, J., W. S. Holbrook, G. M. Kent, P. B. Kelemen, R. S. Detrick, H.-C. Larsen, J. R. Hopper, and T. Dahl-Jensen, 2000, Crustal structure of the southeast Greenland margin from joint refraction and reflection seismic tomography: Journal of Geophysical Research, **105**, no. B9, 21591–21614.

Koulakov, I., 2009a, LOTOS code for local earthquake tomographic inversion: Benchmarks for testing tomographic algorithms: Bulletin of the Seismological Society of America, **99**, 194–214.

———, 2009b, PROFIT code, http://www.ivan-art.com/science/PROFIT, accessed 8 April 2010.

Koulakov, I., M. Bohm, G. Asch, B.-G. Lühr, A. Manzanares, K. S. Brotopuspito, Pak Fauzi, M. A. Purbawinata, N. T. Puspito, A. Ratdomopurbo, H. Kopp, W. Rabbel, and E. Shevkunova, 2007, P and S velocity structure of the crust and the upper mantle beneath central Java from local tomography inversion: Journal of Geophysical Research, **112**, B08310.

Koulakov, I., A. Jakovlev, and B. G. Luehr, 2009a, Anisotropic structure beneath central Java from local earthquake tomography: Geochemistry Geophysics Geosystems, **10**, Q02011.

Koulakov, I., and S. V. Sobolev, 2006, A tomographic image of Indian lithosphere break-off beneath the Pamir Hindukush region: Geophysical Journal International, **164**, 425–440.

Koulakov, I., S. V. Sobolev, M. Weber, S. Oreshin, K. Wylegalla, and R. Hofstetter, 2006, Teleseismic tomography reveals no signature of the Dead Sea Transform in the upper mantle structure: Earth and Planetary Science Letters, **252**, no. 1–2, 189–200.

Koulakov, I., T. Yudistira, B.-G. Luehr, and Wandono, 2009b, *P*, *S* velocity and *VP*/*VS* ratio beneath the Toba caldera complex (northern Sumatra) from local earthquake tomography: Geophysical Journal International, **177**, 1121–1139.

Luetgert, J. H., 1992, MacRay — Interactive two-dimensional seismic raytracing for the Macintosh: U.S. Geological Survey Open-File Report, 92–356.

Martí, D., R. Carbonell, I. Flecha, I. Palomeras, J. Font-Capó, E. Vásquez-Suñé, and A. Pérez-Estaún, 2008, High-resolution seismic characterization in an urban area: Subway tunnel construction in Barcelona, Spain: Geophysics, **73**, no. 2, B41–B50.

Nielsen, C., and H. Thybo, 2009, No Moho uplift below the Baikal rift zone: Evidence from a seismic refraction profile across southern Lake Baikal: Journal of Geophysical Research, **114**, B08306.

Paige, C. C., and M. A. Saunders, 1982, LSQR: An algorithm for sparse linear equations and sparse least squares: Association for Computing Machinery (ACM) Transactions on Mathematical Software, **8**, 43–71.

Palomeras, I., R. Carbonell, I. Flecha, F. Simancas, P. Ayarza, J. Matas, D. Martinez Poyatos, A. Azor, F. Gonzalez Lodeiro, and A. Perez-Estaun, 2009, Nature of the lithosphere across the Variscan orogen of SW Iberia: Dense wide-angle seismic reflection data: Journal of Geophysical Research, **114**, B02302.

Rawlinson, N., and M. Urvoy, 2006, Simultaneous inversion of active and passive source datasets for 3-D seismic structure with application to Tasmania: Geophysical Research Letters, **33**, L24313.

Sager, W. W., and M. S. Pringle, 1987, Paleomagnetic constraints on the origin and evolution of the Musicians and south Hawaiian Seamounts, central Pacific Ocean, *in* B. H. Keating, P. Fryer, R. Batiza, and G. Boehlert, eds., Seamounts, islands, and atolls: American Geophysical Union, 133–162.

Sallarès, V., P. Charvis, E. R. Flueh, and J. Bialas, 2003, Seismic structure of Cocos and Malpelo volcanic ridges and implications for hot spot-ridge interaction: Journal of Geophysical Research, **108**, doi: 10.1029/2003JB002431.

Thurber, C., 1993, Local earthquake tomography: Velocities and Vp/Vs — Theory, *in* H. Iyer, and K. Hirahara, eds., Seismic tomography — Theory and practice: CRC Press, 563–583.

Um, J., and C. Thurber, 1987, A fast algorithm for two-point seismic ray tracing: Bulletin of the Seismological Society of America, **77**, 972–986.

Van der Sluis, A., and H. A. van der Vorst, 1987, Numerical solution of large, sparse linear algebraic systems arising from tomographic problems, *in* G. Nolet, ed., Seismic tomography: D. Reidel, 49–83.

Yordkayhun, S., A. Tryggvason, B. Norden, C. Juhlin, and B. Bergman, 2009, 3D seismic traveltime tomography imaging of the shallow subsurface at the CO_2SINK project site, Ketzin, Germany: Geophysics, **74**, no. 1, G1–G15.

Zelt, C. A., and P. J. Barton, 1998, Three-dimensional seismic refraction tomography: A comparison of two methods applied to data from the Faeroe basin: Journal of Geophysical Research, **103**, 7189–7210.

Zelt, C. A., and R. B. Smith, 1992, Seismic traveltime inversion for 2-D crustal velocity structure: Geophysical Journal International, **108**, 16–34.